The stability and structure of primordial reservoirs in the lower mantle: insights from models of thermochemical convection in three-dimensional spherical geometry

Yang Li,[1] Frédéric Deschamps[2] and Paul J. Tackley[1]

[1]*Department of Earth Sciences, Institute of Geophysics, ETH Zurich, Sonnegstrasse 5, 8092 Zurich, Switzerland. E-mail: yang.li@erdw.ethz.ch*
[2]*Institute of Earth Sciences, Academia Sinica, 128 Academia Road Sec. 2, Nangang, Taipei 11529, Taiwan*

SUMMARY

Large-scale chemical lateral heterogeneities are inferred in the Earth's lowermost mantle by seismological studies. We explore the model space of thermochemical convection that can maintain reservoirs of dense material for a long period of time, by using similar analysis in 3-D spherical geometry. In this study, we focus on the parameters thought to be important in controlling the stability and structure of primordial dense reservoirs in the lower mantle, including the chemical density contrast between the primordial dense material and the regular mantle material (buoyancy ratio), thermal and chemical viscosity contrasts, volume fraction of primordial dense material and the Clapeyron slope of the phase transition at 660 km depth. We find that most of the findings from the 3-D Cartesian study still apply to 3-D spherical cases after slight modifications. Varying buoyancy ratio leads to different flow patterns, from rapid upwelling to stable layering; and large thermal viscosity contrasts are required to generate long wavelength chemical structures in the lower mantle. Chemical viscosity contrasts in a reasonable range have a second-order role in modifying the stability of the dense anomalies. The volume fraction of the initial primordial dense material does not effect the results with large thermal viscosity contrasts, but has significant effects on calculations with intermediate and small thermal viscosity contrasts. The volume fraction of dense material at which the flow pattern changes from unstable to stable depends on buoyancy ratio and thermal viscosity contrast. An endothermic phase transition at 660 km depth acts as a 'filter' allowing cold slabs to penetrate while blocking most of the dense material from penetrating to the upper mantle.

Key words: Composition of the mantle; Dynamics: convection currents, and mantle plumes; Rheology: mantle.

1 INTRODUCTION

Seismological observations indicate that the Earth's lowermost mantle (>2400 km depth) is strongly heterogeneous at a large scale (>1000 km). In particular, two large low shear wave velocity provinces (LLSVPs), in which the shear wave velocity decreases by a few per cent compared to the average mantle, are present beneath the Pacific and Africa (e.g. Su *et al.* 1994; Li & Romanowicz 1996; Ni *et al.* 2002; Wang & Wen 2007; Houser *et al.* 2008; Ritsema *et al.* 2011; He & Wen 2012). Palaeomagnetic reconstructions of the locations of large igneous provinces (e.g. Torsvik *et al.* 2008), and the amplitude of true polar wandering (e.g. Dziewonski *et al.* 2010) suggest that LLSVPs have remained at these locations during at least the past 300 Myr.

The nature of these heterogeneities is still unclear. Several studies (e.g. Schuberth *et al.* 2009, 2012a; Davies *et al.* 2012) argue for a dominantly thermal interpretation, whereas other studies (e.g. Forte & Mitrovica 2001; Karato & Karki 2001; Saltzer *et al.* 2001;

Deschamps & Trampert 2003) prefer a thermochemical interpretation. Several lines of evidence from various data sets, including the anticorrelation between bulk-sound and shear wave velocity anomalies (Ishii & Tromp 1999; Masters *et al.* 2000; Trampert *et al.* 2004; Mosca *et al.* 2012), support a thermochemical origin. It was recently suggested that this anticorrelation may result from wave propagation effects (Schuberth *et al.* 2012b), or might be related to the phase change from perovskite to post-perovskite in the lowermost mantle (Davies *et al.* 2012). Because the anticorrelation between V_S and V_Φ anomalies is also observed by normal mode data (Ishii & Tromp 1999; Trampert *et al.* 2004; Mosca *et al.* 2012), which are not affected by wave propagation effects and further show a correlation between density and seismic velocity anomalies, and because the post-perovskite hypothesis fails to predict large-scale structures, the thermochemical hypothesis appears more likely. The detailed nature of chemical heterogeneities is still under debate, the two main hypothesis being that they result either from the evolution of primordial reservoirs of dense materials formed by differentiation early in the

Earth's early history (e.g. Solomatov & Stevenson 1993; Labrosse *et al.* 2007; Lee *et al.* 2010; Tolstikhin *et al.* 2006), or from accumulation of subducted oceanic crust above the core-mantle boundary (CMB, e.g. Gurnis & Davies 1986; Christensen 1989; Christensen & Hofmann 1994). Recently, it was proposed that small fractions of recycled mid-ocean ridge basalt (MORB) may be episodically incorporated in pre-existing primordial reservoirs (Tackley 2012), which is supported by high-resolution 2-D Cartesian models of convection (Li *et al.* 2014). In this study, we assume that chemical heterogeneities are related to reservoirs of primordial dense material, and we investigate the stability and structure of these primordial reservoirs.

Several studies (e.g. Tackley 1998; Davaille 1999; Tackley 2002; McNamara & Zhong 2004; Oldham & Davies 2004; Deschamps & Tackley 2009) have shown that, the buoyancy ratio (B), measuring the density contrast between the dense and regular materials relative to the density contrast due to thermal expansion, is the most important parameter controlling the stability of the dense material in the mantle. High values of B lead to global chemical stratification in which the dense material covers the entire CMB and the interface is almost horizontal, whereas low values of B leads to rapid mixing. In the case of the Earth's mantle, a global chemical stratification is not desired because it is not observed on 1-D radial seismic models. To avoid stratification and rapid mixing, moderate buoyancy ratio and some additional ingredient are needed. 3-D Cartesian numerical experiments have indicated that a large thermal viscosity contrast allows pools of dense material to be maintained for periods of time comparable to the age of the Earth (Deschamps & Tackley 2008). In contrast, the influence of the volume fraction of dense material was found to be of second order (Jaupart *et al.* 2007; Deschamps & Tackley 2009). The effects induced by an endothermic phase transition at 660 km depth (ringwoodite to perovskite and magnesiowustite) have been studied in various geometries. An interesting effect of this phase transition is to strongly filter the dense material flowing from the lower mantle to the upper mantle (Weinstein 1992; Deschamps & Tackley 2009; van Summeren *et al.* 2009; Deschamps *et al.* 2011).

Here, we extend the systematic search from the previous studies in 3-D cartesian geometry (Deschamps & Tackley 2008, 2009) to spherical geometry, which is the natural geometry of the Earth, by exploring the effects of buoyancy ratio (B), thermal and chemical viscosity contrasts ($\Delta\eta_T$, $\Delta\eta_C$), volume fraction of primordial dense material (X_{vol}), and Clapeyron slope of the 660 km phase transition (Γ_{660}) on the stability and structure of the primordial dense reservoirs.

2 EXPERIMENTAL SETUP

We performed numerical experiments using StagYY (Tackley 2008), which solves the conservation equations of mass, momentum, energy and composition for an anelastic, compressible fluid with infinite Prandtl number. Calculations are performed in 3-D spherical geometry on the Yin-Yang grid (Kageyama & Sato 2004). The grid is radially parametrized on 64 nodes, the radial increment being refined at the top and at the bottom of the mantle. At each depth, the resolution of the Yin (Yang) grid is 64×192 (192×64) points, leading to a total resolution of $64 \times 192 \times 64 \times 2$ points. The curvature of the shell is controlled by the ratio between the core and total radii,

$$f = \frac{r_c}{R}, \tag{1}$$

which we here fix to $f = 0.55$, corresponding to the Earth's mantle's value.

The top and bottom boundaries are free-slip and isothermal. The system is heated both from the bottom and from within, and the heating rate of the primordial material is increased by a factor 10 compared to the regular mantle material, accounting for the fact that MORB source region is depleted in radiogenic elements (Kellogg *et al.* 1999). Compressibility involves depth-dependence of physical properties (density, thermal expansivity and thermal conductivity), and induces additional sources and sinks of heat (viscous dissipation and adiabatic heating/cooling) that are controlled by the dissipation number, Di, which depends on the thermal expansion and thus varies with depth. In our calculations, the surface and volume average value of the dissipation number are $Di_s = 1.2$ and $\langle Di \rangle = 0.39$, respectively. Physical parameters are listed in Table 1.

Viscosity depends on temperature, depth and composition. The depth-dependence consists of an exponential increase with depth, plus a viscosity jump by a factor 30 at a depth of 660 km (corresponding to a non-dimensional height above the CMB $h = z/D = 0.76$). The viscosity is fully described by

$$\eta(z, T) = \eta_0[1 + 29H(0.76 - z/D)] \exp\left[V_a \frac{(1 - z/D)}{D}\right.$$
$$\left. + E_a \frac{\Delta T_S}{(T + T_{off})} + K_a C\right], \tag{2}$$

where η_0 is a reference viscosity, H is the Heaviside step function, T_{off} the temperature offset (here equals to 2200 K) and D the mantle thickness. The viscosity variations with depth and temperature are controlled by V_a and E_a, respectively, modelling the activation volume and energy. Note that, the top to bottom thermal viscosity contrast is defined as $\Delta\eta_T = \exp(E_a)$, but due to the temperature offset, the effective viscosity variations due to temperature variations is smaller than $\Delta\eta_T$. The viscosity variations with composition is controlled by the parameter K_a, the viscosity jump between dense and regular material being $\Delta\eta_C = \exp(K_a)$. To avoid numerical difficulties, the viscosity was truncated between 10^{-5} and 10^5. As an example, we display the viscosity profile for our reference case (Section 3.1) in Supporting Information Fig. S1.

As an input, we define the surface Rayleigh number:

$$Ra_s = \frac{\alpha_s g \rho_s \Delta T_s D^3}{\eta_0 \kappa_s}, \tag{3}$$

where g is the acceleration of gravity, D the mantle thickness and κ_s the surface thermal diffusivity. The surface Rayleigh number remains constant during the entire run, and in all the calculations shown in this paper we prescribed $Ra_s = 10^9$. In contrast, the effective Rayleigh number Ra_{eff} calculated with volume-averaged properties varies with time, but remains in the range of 10^6 to 3×10^6.

Composition is tracked with a collection of Lagrangian tracer particles (Tackley & King 2003). Two types of tracers are used, tracking dense and regular materials, respectively, with a total of 24 million tracers in each experiment. The volume fraction of dense material X_{vol} is varied between 2.5 and 15 per cent. Large values (10 per cent and more) of X_{vol} are unrealistic in the case of the Earth's mantle, and we considered such values only to investigate in details the influence of X_{vol}. The compositional field is obtained by calculating the concentration C of dense tracers in each cell. C varies between 0 for a cell filled with regular material only, and 1 for a cell filled with dense material only. The density difference

Table 1. Parameters and scaling.

Parameter	Symbol	Value	Units	Non-dimensional
Non-dimensional parameters				
Reference Rayleigh number	Ra_s			10^9
Buoyancy ratio	B			0.1–0.5
Volume fraction of dense material	X			0.025–0.15
Initial thickness of the dense layer	h_{DL}			0.05–0.255
Surface dissipation number	Di_S			1.2
Compositional heating ratio	RH_C	10		
Physical and thermodynamical parameters				
Acceleration of gravity	g	9.81	$m\,s^{-2}$	1.0
Mantle thickness	D	2891	km	1.0
Super-adiabatic temperature difference	ΔT_S	2500	K	1.0
Reference adiabat	T_{as}	1600	K	0.64
Surface density	ρ_S	3300	$kg\,m^{-3}$	1
CMB density	ρ_b	4950	$kg\,m^{-3}$	1.5
Density jump at $z = 660$ km	$\Delta\rho_{660}$	400	$kg\,m^{-3}$	0.1212
Surface thermal expansion	α_S	5.0×10^{-5}	K^{-1}	1.0
CMB thermal expansion	α_S	1.0×10^{-5}	K^{-1}	0.2
Surface thermal diffusivity	κ_S	6.24×10^{-7}	$m^2\,s^{-1}$	1.0
CMB thermal diffusivity	κ_b	8.74×10^{-7}	$m^2\,s^{-1}$	1.4
Clapeyron slope at $z = 660$ km	Γ_{660}	−5.0 to 0.0	$MPa\,K^{-1}$	-1.336×10^{-1} to 0.0
Viscosity law				
Reference thermal viscosity	η_0	1.6×10^{20}	Pa s	1.0
Viscosity ratio at $z = 660$ km	$\Delta\eta_{660}$	30		
Thermal viscosity ratio	$\Delta\eta_T$	10^3–10^{10}		
Compositional viscosity ratio	$\Delta\eta_C$	10^{-2}–10^3		
Vertical viscosity ratio	$\Delta\eta_Z$	10^2		
Dimensional scalings				
Velocity	v	1.0	$cm\,yr^{-1}$	1468
Time	t	424	Gyr	1.0
Heat flux	Φ	2.6	$mW\,m^{-2}$	1.0
Interal heating rate	H	2.72×10^{-23}	$W\,kg^{-1}$	1.0

Table 2. Cases used in this study.

Case	B	$\Delta\eta_T$	$\Delta\eta_C$	X_{vol} (per cent)	Γ_{660}	Fig.
1	0.30	10^9	1	3.5	−2.5	1
2–8	0.16–0.50	10^9	1	3.5	−2.5	2, 3, 4
9–13	0.30	10^3–10^{10}	1	5	−2.5	5, 6, 7
14–17	0.20	10^9	1	2.5–15	−2.5	8
18–25	0.30	10^6, 10^9	1	2.5–15	−2.5	9, 10, 11
26–33	0.20, 0.30	10^9	0.03–100	5	−2.5	12, 13
34–39	0.20, 0.30	10^9	1	3.5	0, −2.5, −5	14, 15, 16

between the dense and regular materials is controlled by the buoyancy ratio:

$$B = \frac{\Delta\rho_C}{\alpha_s \rho_s \Delta T_s}, \tag{4}$$

where $\Delta\rho_C$ is the density difference between the dense and regular material, α_s is the thermal expansion at surface, ρ_s is the average density at surface and ΔT_s is the superadiabatic temperature difference across the mantle.

The initial condition for temperature is an adiabatic profile on which thin thermal boundary layers at the top and the bottom, and small random 3-D perturbations are added. The dense material is initially located at the base of the shell in a uniform layer of non-dimensional thickness h_{DL}, which is calculated from the volume fraction of dense material (X_{vol}) and the geometry (f).

$$h_{DL} = \frac{[X_{vol}(1 - f^3) + f^3]^{1/3} - f}{1 - f}. \tag{5}$$

To estimate the time of the onset of instability of the dense layer, we use the method defined in Deschamps & Tackley (2008), which is based on the evolution of the average non-dimensional altitude of dense material:

$$\langle h_c \rangle = \frac{1}{V} \int_V C(r, \theta, \phi) r \, dV. \tag{6}$$

For stable layering, $\langle h_c \rangle$ remains constant in time at $a \times h_{DL}$, (where a is a geometrical constant depending on the curvature of the shell), and h_{DL} is the initial thickness of the dense layer. As the layer gets unstable, $\langle h_c \rangle$ increases. More importantly, $\langle h_c \rangle$ is a good measure of the degree of mixing of the system at each stage of the experiment. Values of $\langle h_c \rangle$ around $a \times h_{DL}$ indicates stable layering, whereas for efficient mixing one gets

$$\langle h_c \rangle = \frac{\left(\frac{1 + f^3}{2}\right)^{1/3} - f}{1 - f}. \tag{7}$$
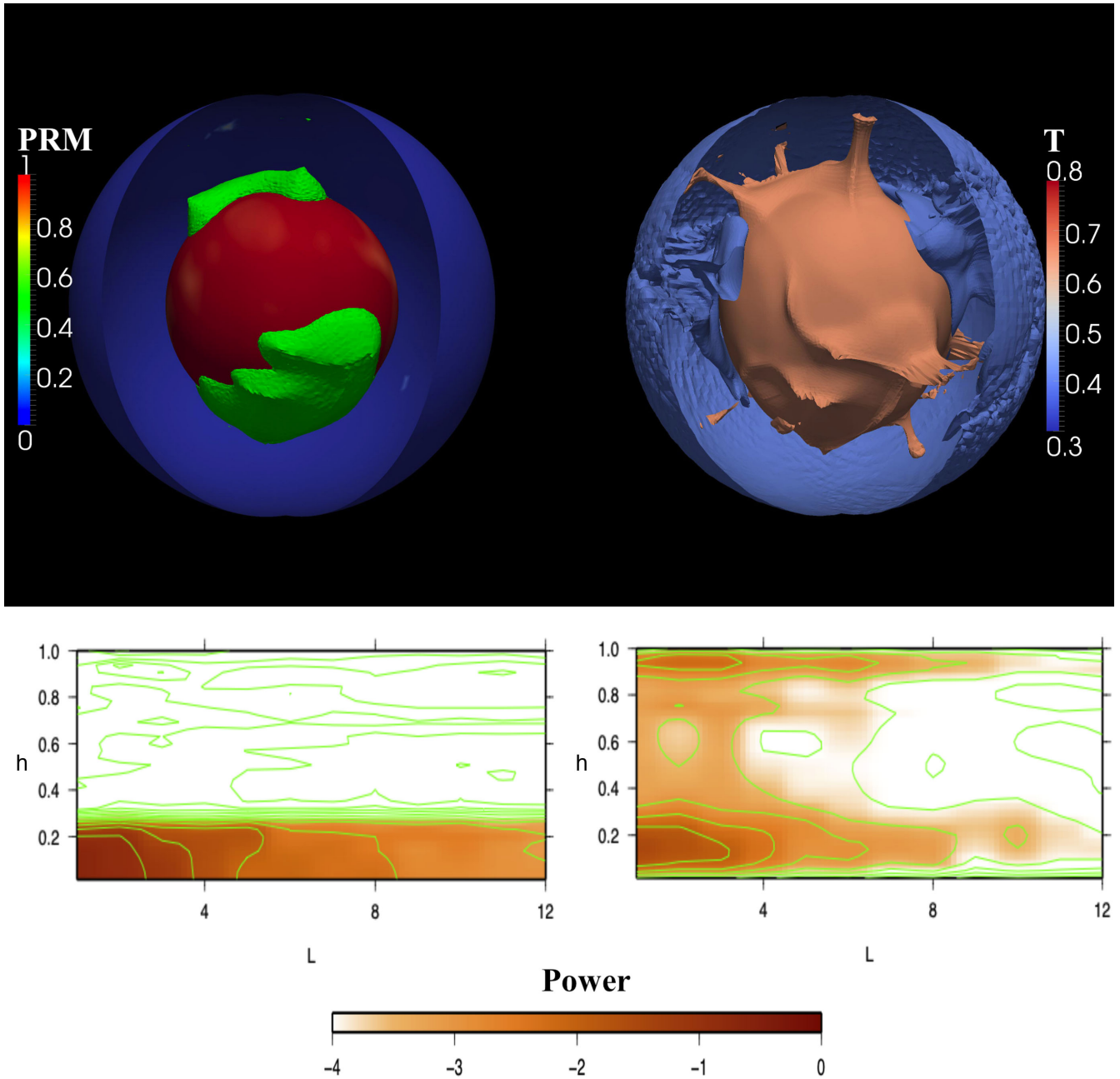
Figure 1. Snapshot of reference case with $B = 0.30$, $\Delta\eta_T = 10^9$, $\Delta\eta_C = 1$, $X_{vol} = 3.5$ per cent at time 4.5 Gyr. Top row: isosurface of the composition with contour level $C = 0.50$ (left). Isosurface of the non-dimensional temperature with contour level $T = 0.65$ and $T = 0.40$ (right). Bottom row: SHM of composition field up to degree 12 (left). SHM of temperature field up to degree 12 (right).

For $f = 0.55$, this leads to $\langle h_c \rangle = 0.634$. Stable reservoirs of dense material lead to intermediate values of values of $\langle h_c \rangle$.

3 RESULTS

3.1 Reference case

For comparisons, we define a reference case (here, referred to as case 1) with the following properties: a buoyancy ratio of 0.30, corresponding to a density contrast of 120 kg m^{-3} and a viscosity that varies both with depth ($V_a = 4.603$) and with temperature ($E_a = 20.723$). The chemical viscosity contrast is set to 1, that is

the dense material and regular material have the same viscosity, all other parameters being the same. At the upper/lower mantle boundary we impose a viscosity jump of factor 30, and a phase transition with a non-dimensional Clapeyron slope of -0.0668, corresponding to -2.5 MPa K^{-1}. The initial volume fraction of primordial dense material is 3.5 per cent.

In this reference case, after the onset of the convection two large reservoirs of dense material are generated at the bottom of the shell and survive convection (Fig. 1a). The power spectrum of chemical anomalies is dominated by large-scale structures, that is low spherical harmonic degrees (Fig. 1b). The dense reservoirs can survive mantle convection (i.e. they are not re-entrained by the flow) for a period of time larger than the age of the Earth. Plumes are generated
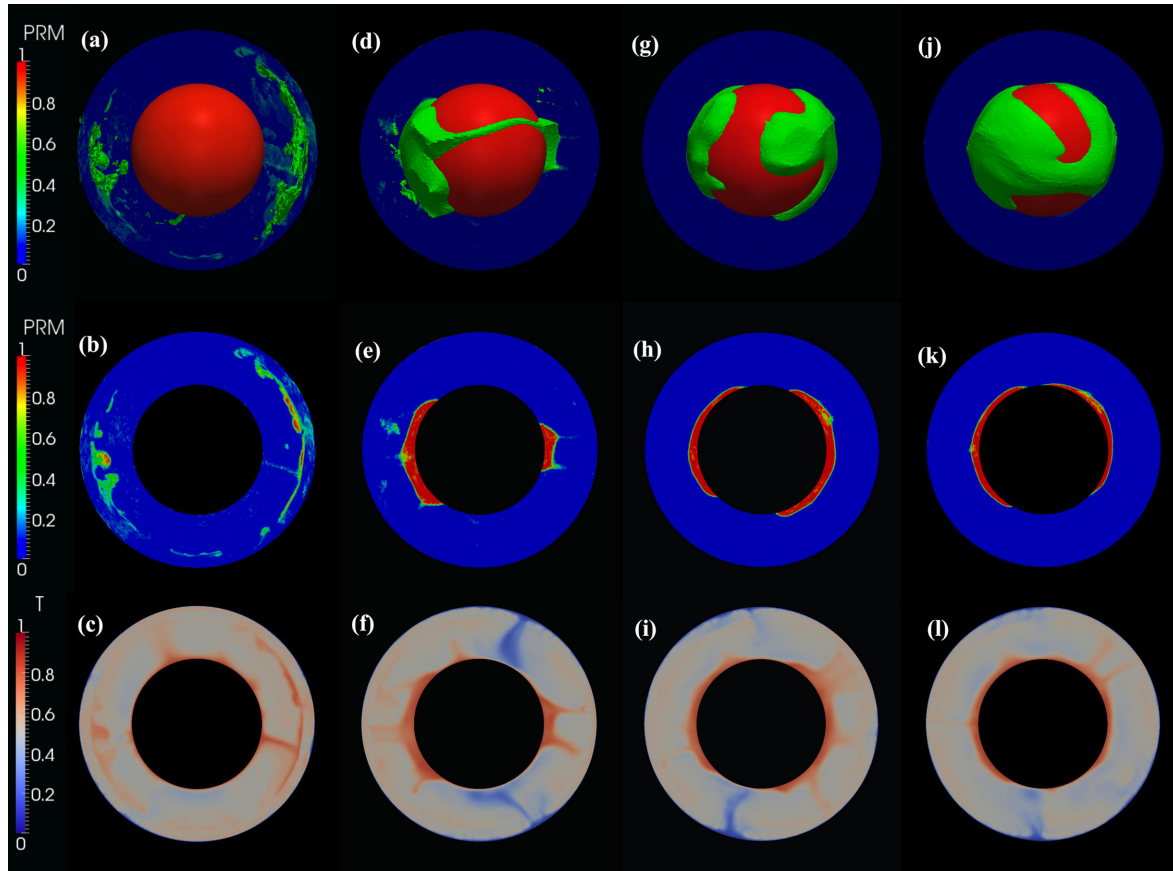
Figure 2. Snapshot of cases with (from left to right): $B = 0.16$, 0.26, 0.36, 0.50, $\Delta\eta_T = 10^9$, $\Delta\eta_C = 1$, $X_{vol} = 3.5$ per cent, $\Gamma_{660} = -2.5$ MPa K^{-1}. Top row: isosurface of the composition with contour level $C = 0.5$. Middle row: polar slices of the composition. Bottom row: polar slices of temperature.

at the top of these reservoirs and entrain small fractions of dense material. This erosion is however very small. We extended the calculation to 9 billion years and the reservoirs in the lower mantle were still present, with a similar structure as in Fig. 1. An interesting difference, compared to similar calculations in 3-D Cartesian geometry (Deschamps & Tackley 2008, 2009), is that many plumes are located on the edges of the reservoirs. This is consistent with the observation that most of the deep rooted hotspots are generated on the edges of the low shear wave velocity provinces (e.g. Torsvik *et al.* 2008), and with previous models of thermochemical convection (e.g. Tan *et al.* 2011).

The flow pattern is time dependent. After they formed, plumes remain the same position for some period of time. They then disappear and are replaced by newly formed plumes located elsewhere. At each time step, however, most of the plumes are located at the margins instead of the central area of the dense reservoirs. The detailed location of plumes is likely related to the detailed dynamics of the dense reservoirs, and the temperature distribution within them. In addition, cold downwellings arriving at the bottom of the shell play an important role by pushing away chemical piles. A full understanding of the plume distribution at the top of the dense reservoirs requires a detailed study of the dynamics of these reservoirs, which is beyond the scope of this paper.

3.2 Effects of buoyancy ratio

We present a series of experiments with the buoyancy ratio between 0.1 and 0.5 (cases 2 to 8). According to the parameters listed in

Table 1, this leads to density contrasts between 41 and 206 kg m^{-3}. Other parameters are the same as in the reference case.

We observe significant changes in the stability and structure of the system, depending on B. For buoyancy ratios smaller than 0.20, the dense material is quickly swept around by mantle convection (Fig. 2a), and entrained upwards in the shell. Dense and regular material mix efficiently after the onset of convection. The thermal structure is dominated by large plumes that are generated at the bottom of the shell, rise upwards and spread out beneath the phase transition (Fig. 2c). Above this transition, secondary plumes rising up to the surface are generated.

For intermediate buoyancy ratios ($B = 0.20$–0.36), large thermochemical reservoirs are generated at the bottom of the shell and remain stable for periods of time comparable to the age of the Earth. Clearly, the thermochemical structure varies strongly with B (Figs 2d–i). Dense reservoirs have substantial topography for cases with smaller B (around 0.2–0.3), while the dense material tends to flatten and spread above the CMB with increasing B. Despite their different shapes, these structures are dominated by long wavelengths, as indicated by spectral heterogeneity maps (Fig. 3). After they have formed, these long wavelengths thermochemical structures remain stable during the rest of the experiments.

For larger buoyancy ratios (>0.36), reservoirs remain stable during the whole run time without forming large topography structures, but with no ubiquitous layer surrounding the core, due to the small fraction of dense material ($X_{vol} = 3.5$ per cent) used in these experiments (Fig. 2j–l). A fully core-covering dense layer can be obtained only with both a large buoyancy ratio ($B > 0.4$) and a large volume

composition
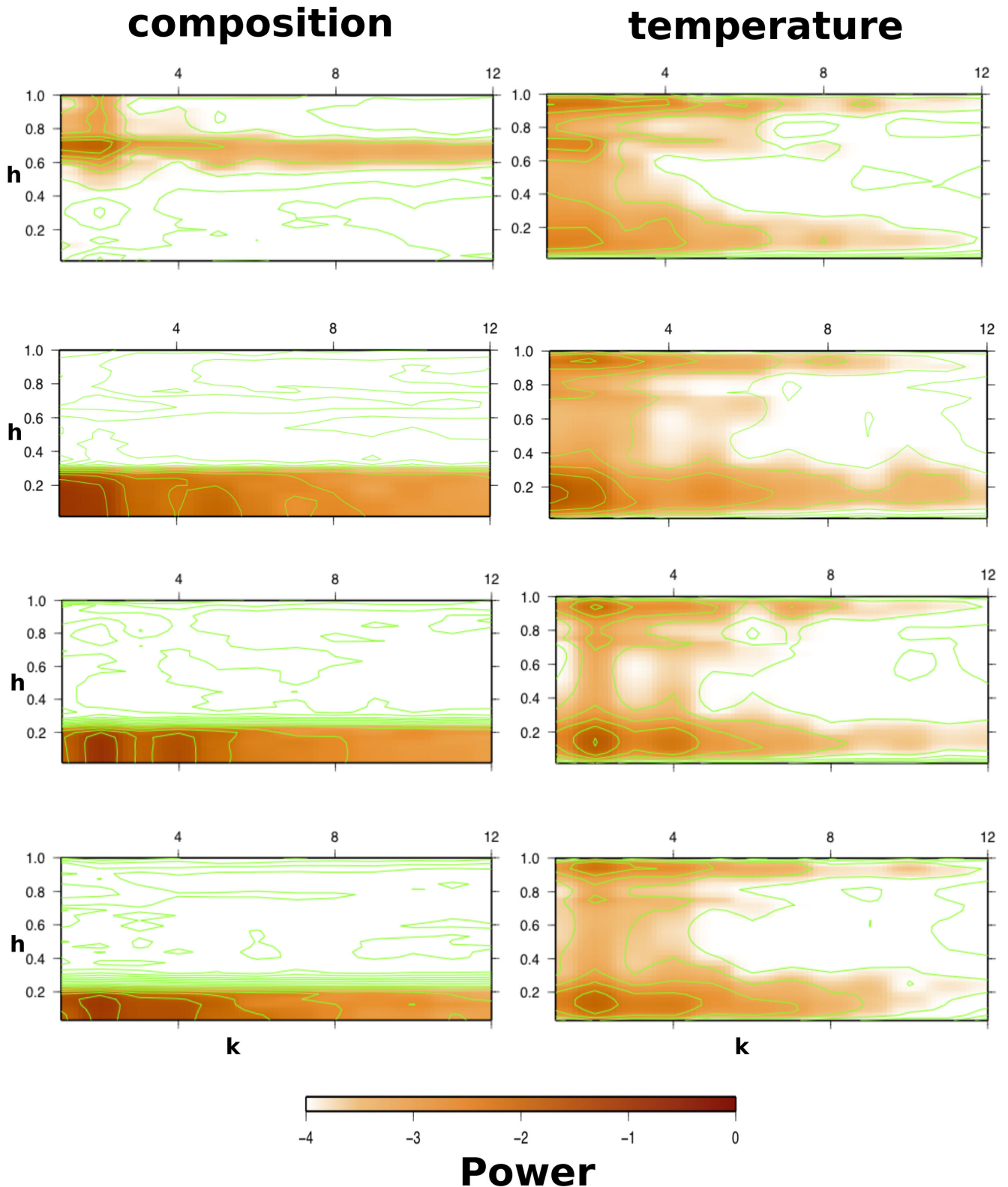
temperature

Figure 3. Spectral heterogeneity map (SHM) of the temperature (left column), and composition (right column) for the four cases show in Fig. 2. From top to bottom: $B = 0.16$, $B = 0.26$, $B = 0.36$, $B = 0.50$.

fraction ($X_{vol} > 10$ per cent; Section 3.4). If such global layering were present in the Earth's mantle, it would induce a discontinuity near the bottom of the mantle, in contradiction with 1-D radial seismic profiles (e.g. Dziewonski & Anderson 1981; Kennet 1991).

This series of experiments indicates that, as observed in Cartesian geometry (Tackley 1998; Davaille 1999; Jaupart *et al.* 2007; Deschamps & Tackley 2009), the buoyancy ratio is the main parameter controlling the stability of the dense material. Low values
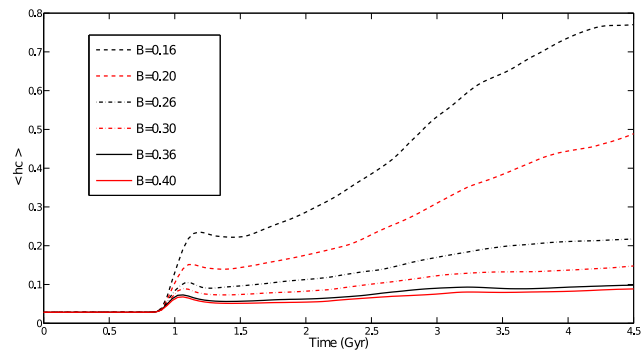
Figure 4. Influence of buoyancy ratio. Average depth of dense material, $\langle h_c \rangle$ as a function of time and for various values of B, including the three cases in Fig. 2.

of this parameter lead to efficient mixing of the initial dense layer with the rest of the shell, whereas large values induce stable layering (Figs 2–4).

Note that B as defined in this paper uses the thermal expansivity at the top of the mantle, which is five times larger than the thermal expansivity at the base of the mantle (Table 1). If B were instead defined using thermal expansivity at the base of the mantle, which is where the balance between thermal and compositional buoyancy matters in our experiments, then the boundary between rapid layer overturn and long-term stable reservoirs occurs at a B of around 1.0, as expected from previous works in which expansivity was not depth dependent. For further discussions on this see (e.g. Tackley 1998).

3.3 Effects of the thermal viscosity contrast

In cases 9–13, we performed runs with values of E_a from 0 to 23.03, which potentially correspond to thermal viscosity contrast ($\Delta \eta_T$) from 1 to 10^{10}. However, due to the temperature offset (eq. 2), the effective thermal viscosity contrast is lower, which avoids the system operating in stagnant-lid mode. Instead, the system is in a sluggish lid regime which tends to generate long wavelength convection (Tackley *et al.* 1993; Tackley 1996). The buoyancy ratio was fixed at $B = 0.30$. Again, strong changes in the thermochemical structure are observed, depending on the value of $\Delta \eta_T$ (Fig. 5).

First, it should be noted that the onset time of mantle convection (t_{onset}) increases with the thermal viscosity contrast ($\Delta \eta_T$) (Fig. 7). Meanwhile, the stability of dense reservoirs increases with increasing thermal viscosity contrast. For thermal viscosity contrasts smaller than 10^6, the layer of dense material becomes unstable after a non-dimensional time of less than 10^{-3} (Fig. 7). Dense material is swept upwards, and quickly mixes with the regular material (plots a,b,d and e in Fig. 5). For thermal viscosity contrasts larger than 10^8, reservoirs of dense material are generated and remain stable in the lower mantle during the entire run.

For intermediate thermal viscosity contrasts in the range 10^6–10^8, the onset time of the convection is larger than in cases with small thermal viscosity contrasts, and the structure of dense reservoirs is substantially different. Fig. 5 indicates that smaller thermal viscosity contrast leads to sharp edges at the boundary, whereas for larger thermal viscosity contrast, the dense reservoirs are flatter and cover a larger fraction of the CMB. Also, the mixing of the dense material and regular material becomes less efficient with increasing thermal viscosity contrast.
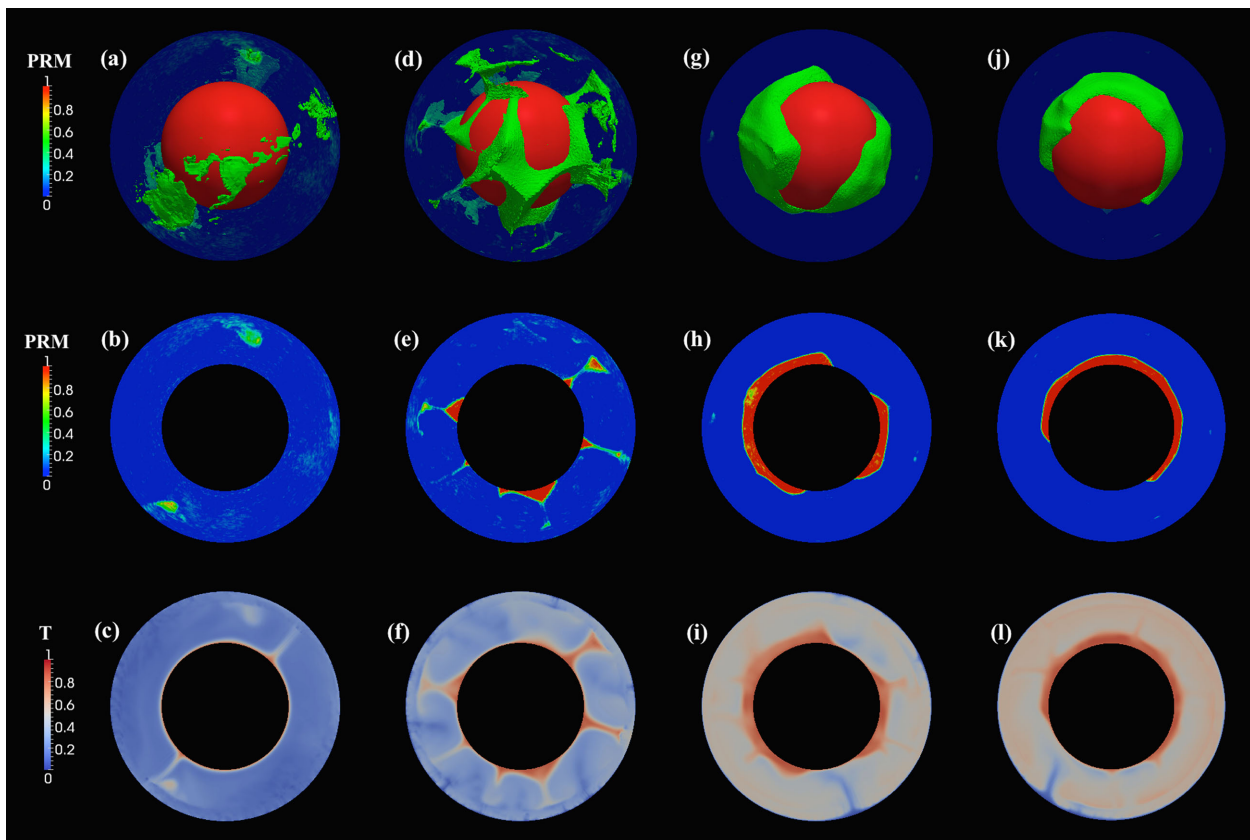
Figure 5. Snapshot for cases with $B = 0.30$, $X_{\mathrm{vol}} = 5$ per cent, $t = 0.0117$ (4.5 Gyr) and (from left to right): $\Delta \eta_T = 10^3$, 10^6, 10^9, 10^{10}. Top row: isosurface of composition with contour level $C = 0.5$. Middle row: polar slice of composition. Bottom row: polar slice of temperature.

composition

temperature
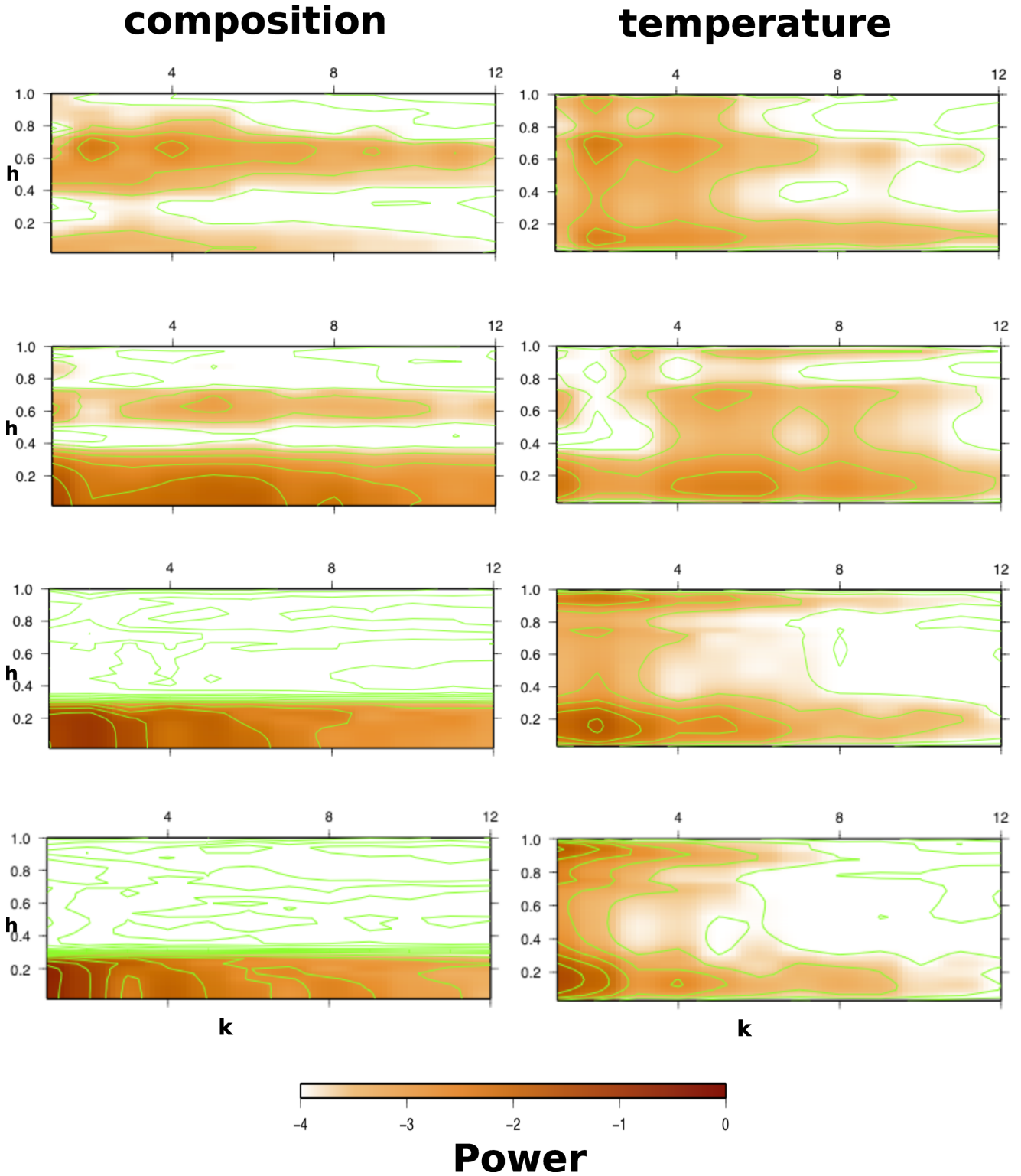
Figure 6. Spectral heterogeneity maps (SHM) of the composition for cases with $B = 0.30$, $X_{vol} = 5$ per cent and (a) $\Delta\eta_T = 10^3$, (b) $\Delta\eta_T = 10^6$, (c) $\Delta\eta_T = 10^9$, (d) $\Delta\eta_T = 10^{10}$.

Fig. 6, which shows spectral heterogeneities maps (SHM) of the compositional field, indicates that long wavelength structures are more easily generated with large $\Delta\eta_T$. In contrast, the cases with small $\Delta\eta_T$ are dominated by short wavelength structures.

Furthermore, increasing thermal viscosity contrast flattens the topography of the dense reservoirs (Fig. 7), an observation that

agrees with previous studies (Bower *et al.* 2013). The thermal viscosity contrast thus has a strong influence on the stability and shape of reservoirs of dense material. Large contrasts, corresponding to a strongly temperature-dependent viscosity, are needed to maintain reservoirs of dense material in the lower mantle. This is consistent with results obtained in 3-D Cartesian geometry (Deschamps &
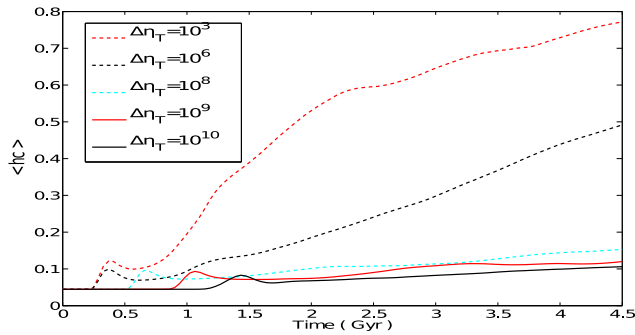
Figure 7. Influence of the thermal viscosity contrast. Plotted is the average depth of the dense material $\langle h_c \rangle$ as a function of time for cases with $B = 0.30$, $X_{vol} = 5$ per cent and various values of $\Delta \eta_T = 10^3, 10^6, 10^8, 10^9, 10^{10}$.

Tackley 2008). An important difference is that larger contrasts are needed in spherical geometry than in 3-D Cartesian geometry. Our study indicates that contrasts in the range 10^8–10^{10} (which refers to E_a between 18.42 and 23.03), maintain stable reservoirs more easily and are therefore more likely for the Earth's mantle.

Taking $\Delta T_S = 2500$ K and $R = 8.32$, the thermal viscosity contrast we imposed in our reference case ($E_a = 20.723$) is equivalent to an activation energy of about 435 kJ mol^{-1}. Thermal viscosity contrasts of 10^8 and 10^{10} correspond to activation energies of 390 and 480 kJ mol^{-1}, respectively, which are in the range of deep mantle activation energies for MgO and perovskite derived by Yamazaki & Karato (2001) as well as the top-of-lower-mantle value for perovskite measured by Holzapfel *et al.* (2005), but lower than *ab initio* calculations for perovskite determined by Ammann *et al.* (2009).

## 3.4 Effects of volume fraction of dense material

In cases 14 to 25, we performed experiments with fixed buoyancy ratio and thermal viscosity contrast, but varied the volume fraction of dense material from 2.5 per cent, which is representative of the LLSVP volume (e.g. Hernlund & Houser 2008), to 15 per cent. Note that large values of volume fraction (>10 per cent) are not realistic for the Earth's mantle, but we consider them to better understand the influence of this parameter.

For small thermal viscosity contrast (<10^6) and/or small buoyancy ratio (<0.20), the layer of dense material becomes unstable and is swept into the upper mantle quickly after the onset of convection, whatever the volume fraction we imposed. In contrast, for large thermal viscosity contrast (>10^8), changing the volume fraction does not substantially modify the stability and structure of the reservoirs of dense material (e.g. cases with $B = 0.30$, $\Delta \eta_T = 10^9$ for which only $\langle h_c \rangle$ are plotted in Fig. 10).

For intermediate thermal viscosity contrasts (between 10^6 and 10^8), the volume fraction of dense material plays a role, although a second-order role compared to that of the buoyancy ratio. Indeed, a comparison between Figs 8 and 9 indicates that the volume fraction of dense material has a stronger influence on the stability and structure of dense reservoirs when the buoyancy ratio is lower.

Our results also show that with a small volume fraction of dense material (i.e. $X_{vol} < 3.5$ per cent), it may be very difficult to get a stable layer of dense material fully covering the CMB, because the cold downwellings which subduct to the deep mantle are strong enough to break and push aside the dense material.

An interesting difference, compared to calculations in 3-D Cartesian geometry (Deschamps & Tackley 2009) is the distribution of
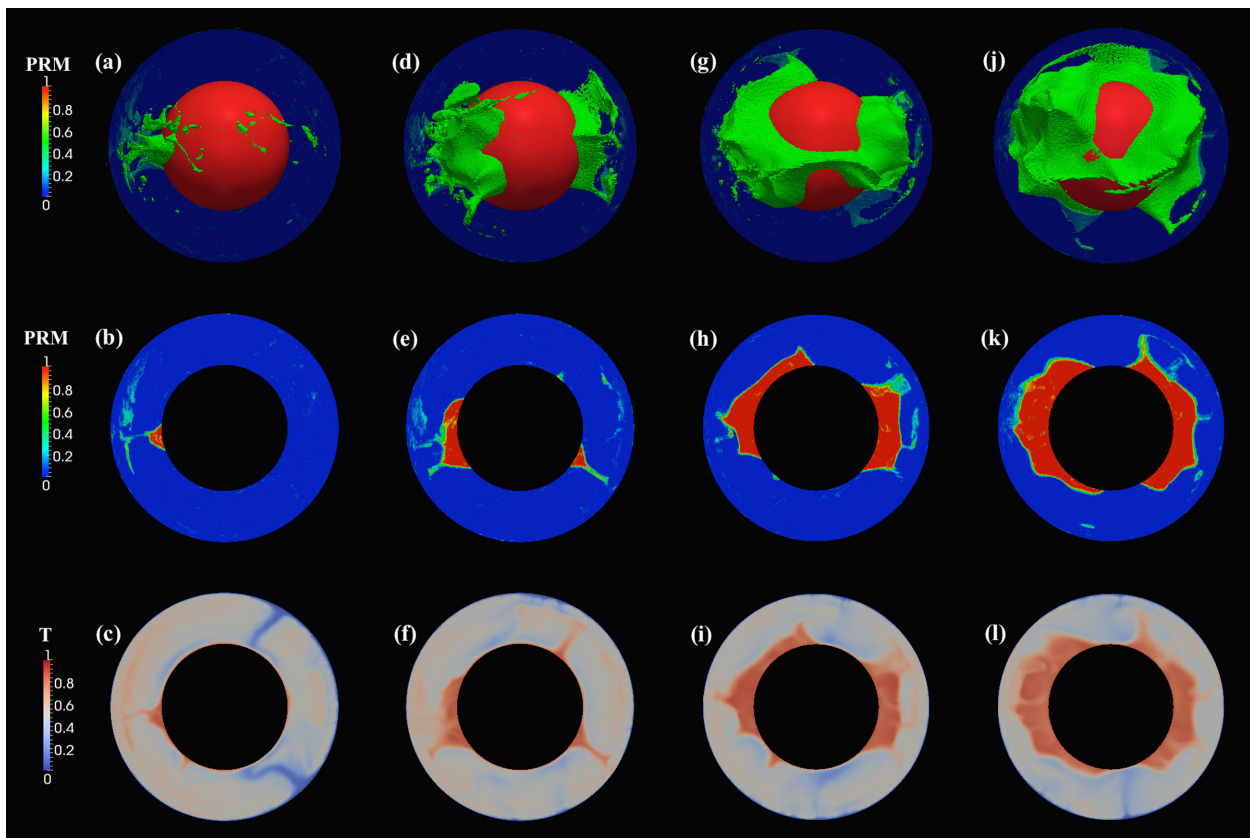
Figure 8. Snapshot of cases with $B = 0.20$, $\Delta \eta_T = 10^9$, $t = 0.0117$ (4.5 Gyr) and (from left to right): $X_{vol} = 2.5, 5, 10, 15$ per cent. Top row: isosurface of the composition with contour level $C = 0.5$. Middle row: polar slice of composition. Bottom row: polar slice of non-dimensional temperature.
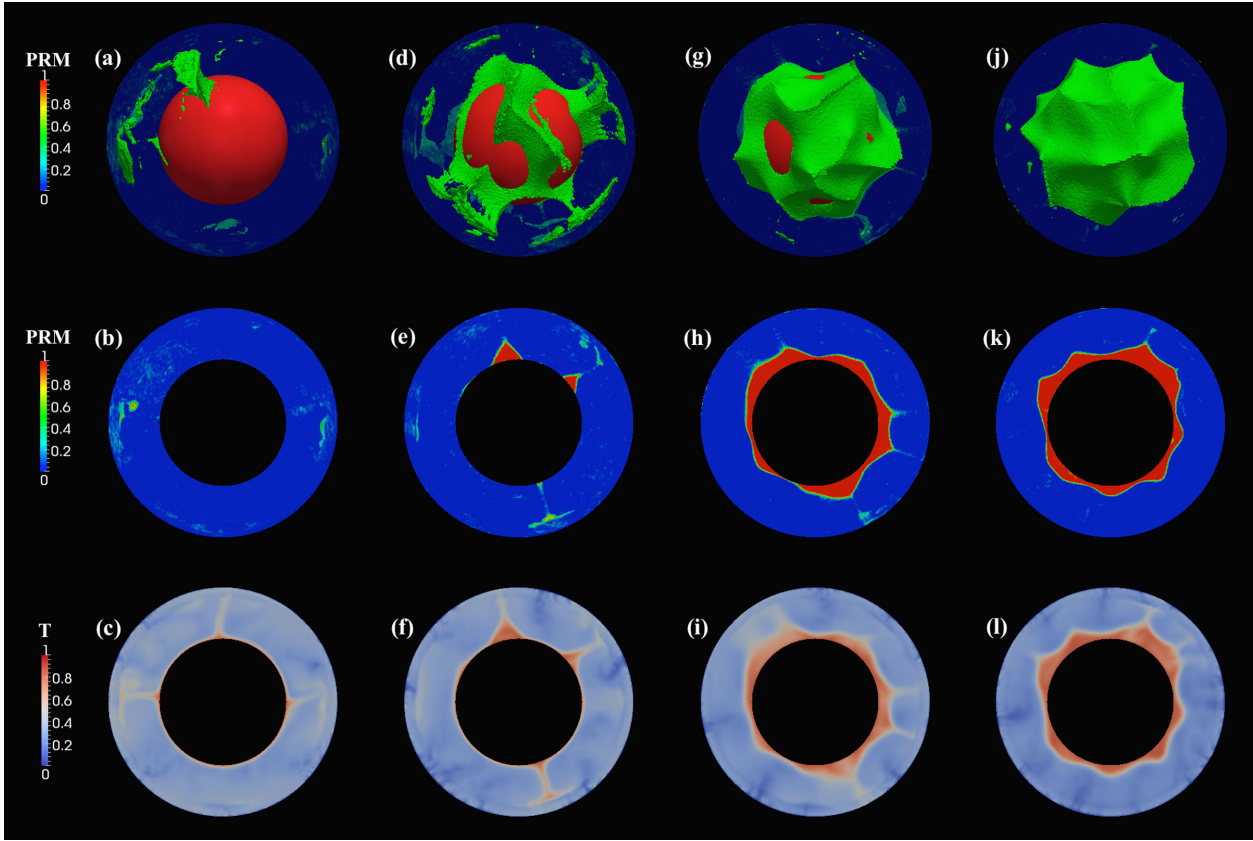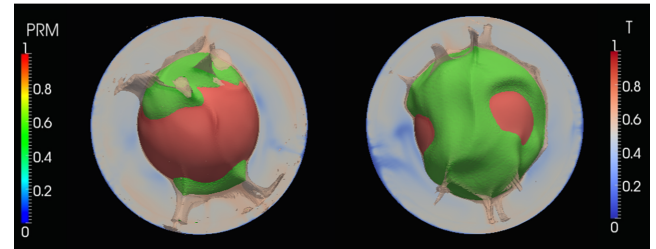
Figure 9. Snapshot of cases with $B = 0.30$, $\Delta\eta_T = 10^6$, $t = 0.0117$ (4.5 Gyr) and (from left to right): $X_{vol} = 2.5$, 5, 10, 15 per cent. Top row: isosurface of the composition with contour level $C = 0.5$. Middle row: polar slice of composition. Bottom row: polar slice of non-dimensional temperature.
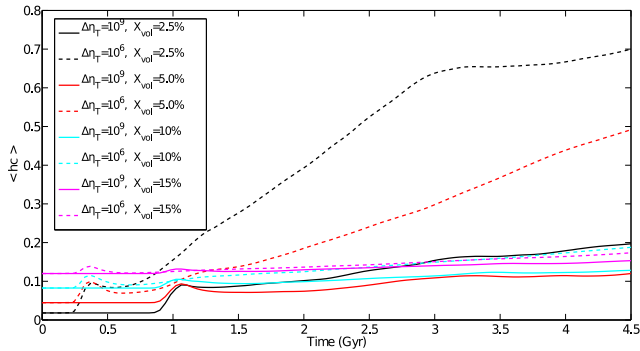
Figure 10. Influence of volume fraction of dense material. All cases have $B = 0.30$. Average depth of dense material, $\langle h_c \rangle$ as a function of time for various values of volume fraction (X_{vol}) and the thermal viscosity contrast ($\Delta\eta_T$), including the cases in Fig 9.

Figure 11. Snapshot of cases with $B = 0.30$, $\Delta\eta_T = 10^9$, $t = 0.0117$ (4.5 Gyr) and (from left to right): $X_{vol} = 3.5$, 10 per cent. A combination of isosurface of the composition $C = 0.5$ and non-dimensional temperature $T = 0.6$ to show the locations of the hot plumes from the dense reservoirs.

the plumes. First, it should be noted that in both geometries, the locations of plumes are related to the dense reservoirs (i.e. we do not observe plumes rising from locations outside these reservoirs), regardless of the volume fraction of dense material. However, in 3-D Cartesian calculations, most of the plumes rise from the area located in the central region of the dense reservoirs. In our calculations, by contrast, the locations of plumes strongly depend on volume fraction of dense material (Fig. 11). For a large volume fraction (e.g. 10 per cent or larger), plumes are mostly located on the central area of these reservoirs. In contrast, for volume fractions lower than 5 per cent, most of plumes are located on the edges of the dense reservoirs, and only a few plumes still rise from the central

parts. This is consistent with the observations that the reconstructed positions of large igneous provinces are preferentially located at the margins of the LLSVPs (e.g. Torsvik *et al.* 2006). However, it is also important to note that all plumes do not necessarily rise from the edges of LLSVPs. Our experiments show that plumes may also be generated within dense reservoirs, and reconstructed LIPs do not all fit on the margins of LLSPVs, but may also found within the LLSVPs. A recent analysis (Austermann *et al.* 2014) further suggest that there is no significant correlation between the locations of plumes and margins of LLSVPs. Finally, thermal winds may slightly shift the surface expression of hotspots away from their root in the deep mantle (Fig. 11). However, a full understanding of the plume distribution requires studying the coupled dynamics of dense reservoirs and cold downwellings in more detail, which is beyond the scope of this study.

3.5 Effects of the chemical viscosity contrast

Another parameter controlling the rheology of the fluid is the chemical viscosity contrast between dense and regular materials, which may influence the detailed shape of the reservoir (Deschamps & Tackley 2008). In cases 26–33, we performed experiments in which the chemical viscosity contrast is varied between 0.03 and 100.

For cases with a small buoyancy ratio ($B = 0.20$) and large thermal viscosity contrast (10^9), the chemical viscosity contrast has a substantial influence on the thermochemical structure of the system (Fig. 12). The dense reservoirs have larger topography with increasing value of $\Delta\eta_C$. Note that in the cases shown in Fig. 12, because the buoyancy ratio is relatively small, the reservoirs are not very stable. For cases with a larger buoyancy ratio ($B = 0.30$), dense reservoirs are more stable and the chemical viscosity contrast plays only a second-order role (Fig. 13). Additional calculations with $B = 0.30$ show that dense reservoirs become unstable only for smaller values of the thermal viscosity contrast (around 10^4) and smaller values of the chemical density contrast (10^{-1}).

This series of experiments indicates that the chemical viscosity contrast plays a second-order role on the stability of the dense reservoirs. It however slightly modifies the shape of the reservoirs by controlling its detailed topography, with both the topography and the steepness of the reservoirs increasing with increasing $\Delta\eta_C$ (Fig. 12).

## 3.6 Effects of the phase transition at 660 km depth

Because it opposes the cold downwellings and hot upwellings, an endothermic phase transition, such as the spinel-to-perovskite and periclase/wustite transition at 660 km depth, is likely to have a strong effect on the mantle flow pattern. Models of thermal convection indicate that slabs may penetrate below an endothermic phase transition through episodic avalanches (e.g. Machetel & Weber 1991; Tackley *et al.* 1993; Wolstencroft & Davies 2011). Experiments in 2-D Cartesian geometry have further suggested that if its Clapeyron slope is large enough, an endothermic phase transition may induce compositional layering by trapping dense material below the phase transition (Weinstein 1992). More recently, several models have pointed out that the 660 km discontinuity acts as a filter for dense material entrained by hot plumes (Deschamps & Tackley 2009; van Summeren *et al.* 2009; Deschamps *et al.* 2011). The detail effect of the 660 km phase transition on plumes is however still debated, due to the multiple phase change occurring at these depths. It has for instance been pointed out that hot material may go through an exothermic phase transition at 660 km (Hirose 2002). In cases 34–39, we performed a series of experiments with a Clapeyron slope (Γ_{660}) between 0 and -5 MPa K^{-1}, corresponding to non-dimensional values between 0 and -0.1336 (Figs 14 and 15). Note that in all experiments we impose a viscosity jump of 30 at the phase transition.

In models with a small buoyancy ratio ($B = 0.20$), in which the layer of dense material is unstable, and a Clapeyron slopes between 0 and -1.25 MPa K^{-1}, the dense material entrained by plumes crosses the 660-km phase transition without significant filtering. When the Clapeyron slope is set to 0, plumes remain unaffected and a substantial part of the dense material is entering the upper mantle (Fig. 14a and b). With increasing magnitude of Clapeyron slope, the plumes spread out below the phase transition. Small secondary plumes are generated above the transition and rise towards the surface. Most of the dense material is trapped below the transition zone, but a small fraction is entrained above this transition
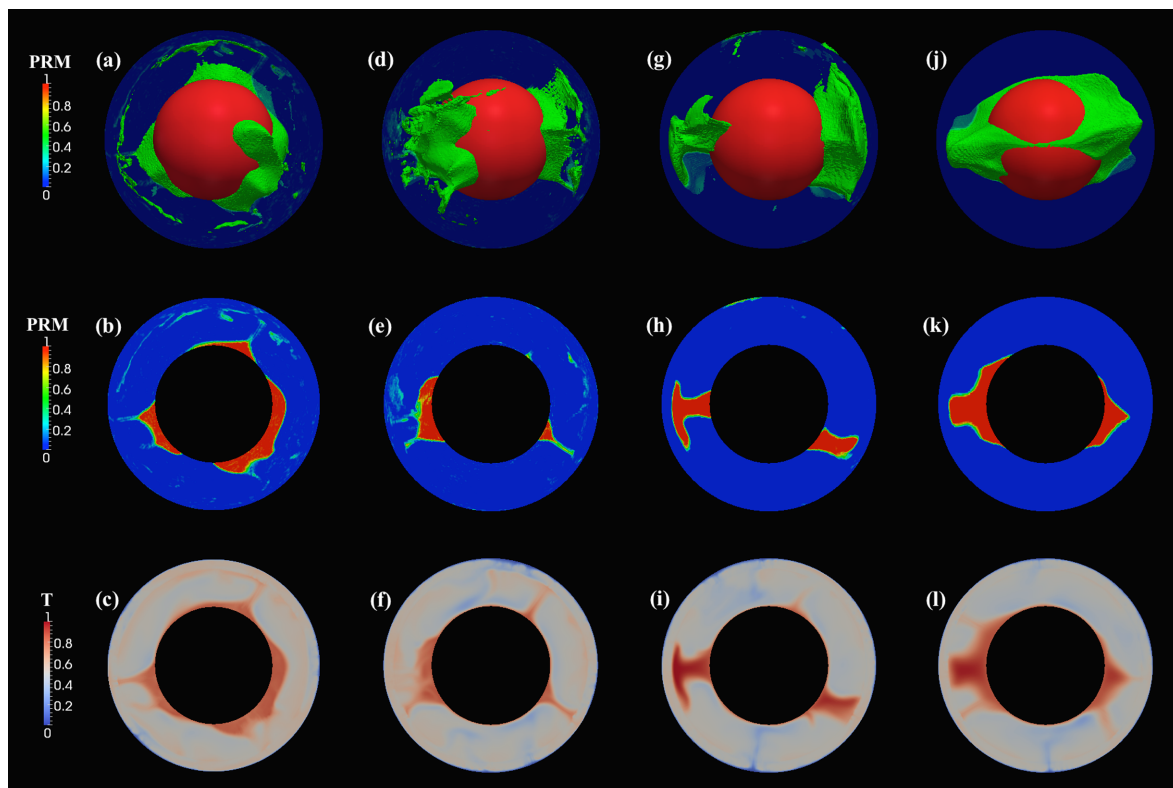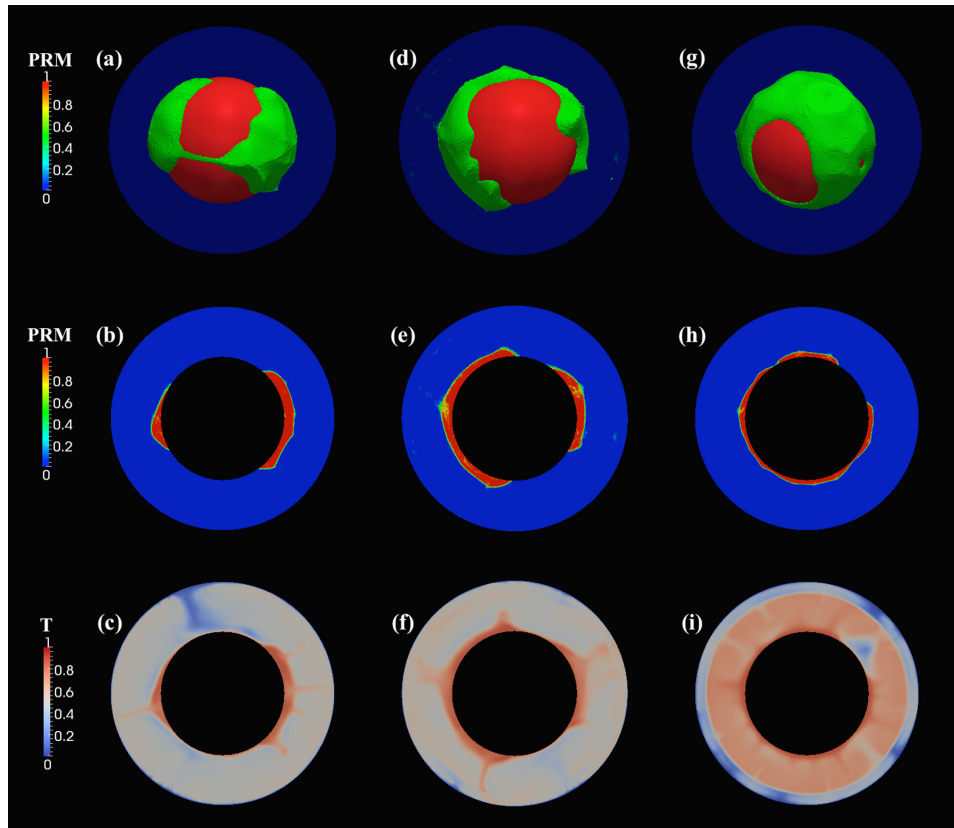
Figure 12. Snapshot of cases with $B = 0.20$, $X_{vol} = 3.5$ per cent, $\Delta\eta_T = 10^9$, $t = 0.0117$ (4.5 Gyr) and (from left to right): $\Delta\eta_C = 0.03, 1, 30, 100$. Top row: isosurface of the composition with contour level $C = 0.5$. Middle row: polar slice of the composition. Bottom row: polar slice of the temperature.
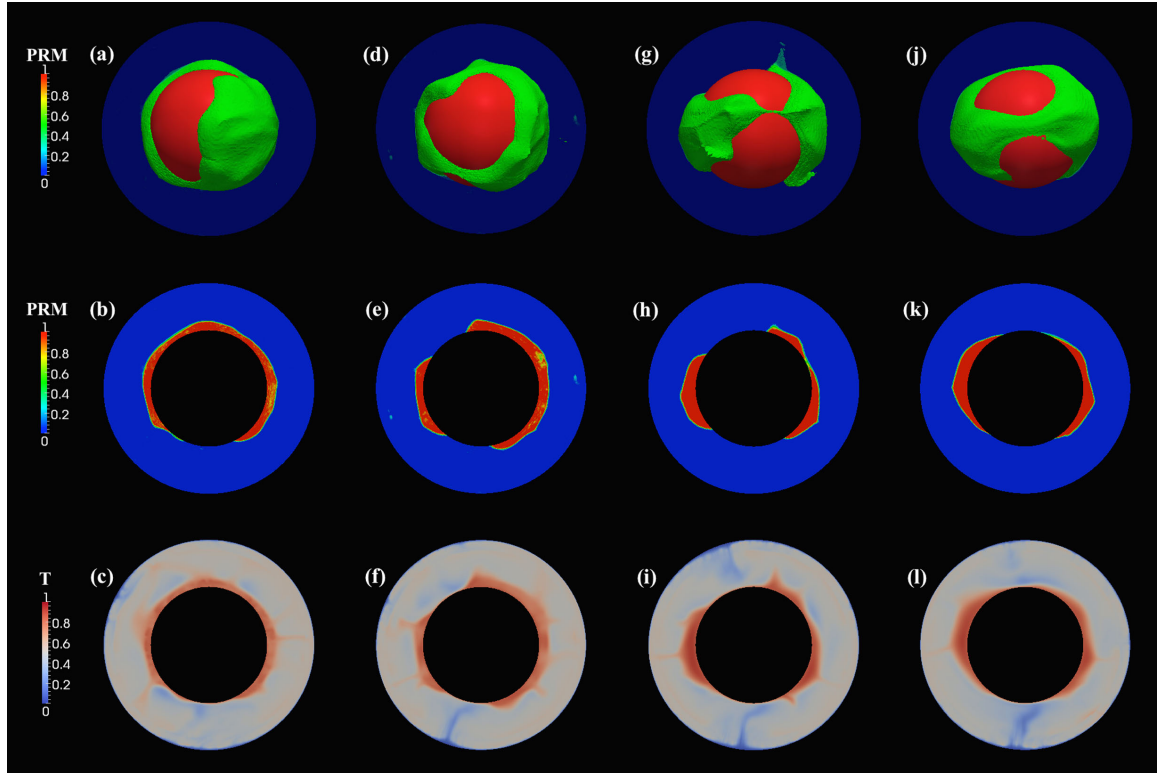
Figure 13. Snapshot of cases with $B = 0.30$, $\Delta\eta_T = 10^9$, $X_{vol} = 3.5$ per cent, $t = 0.0117$ (4.5 Gyr) and (from left to right): $\Delta\eta_C = 0.03, 1, 30, 100$. Top row: isosurface of the composition with contour level $C = 0.5$. Bottom row: polar slice of the non-dimensional temperature.
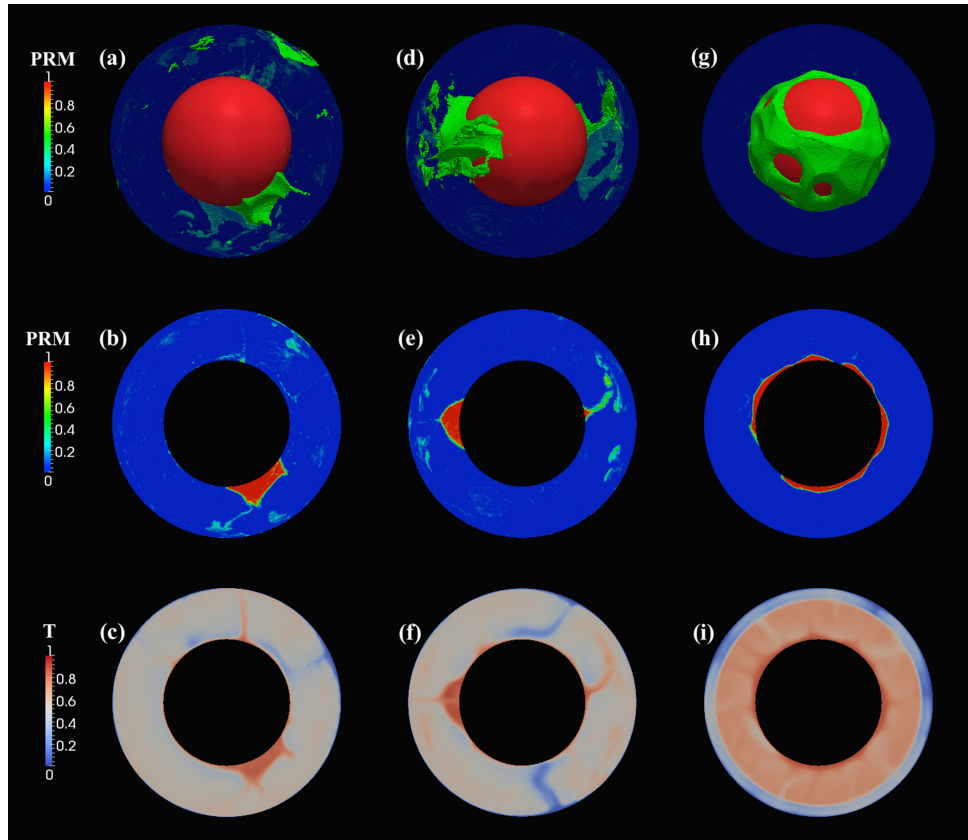
Figure 14. Snapshot of cases with $B = 0.20$, $X_{vol} = 3.5$ per cent, $\Delta\eta_T = 10^9$, $t = 0.0117$ (4.5 Gyr) and (from left to right): 660 km Clapeyron slope (Γ_{660}) = 0, −2.5, −5 MPa K^{-1}. Top row: isosurface of the composition with contour level $C = 0.5$. Middle row: polar slice of the composition. Bottom row: polar slice of the temperature.
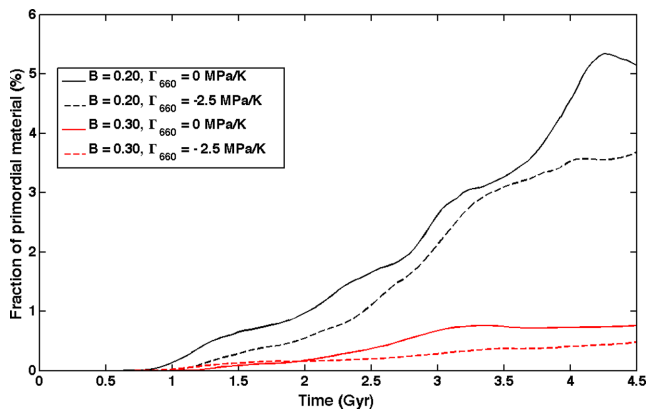
Figure 15. Snapshot of cases with $B = 0.30$, $X_{vol} = 3.5$ per cent, $\Delta\eta_T = 10^9$, $t = 0.0117$ (4.5 Gyr) and (from left to right): 660 km Clapeyron slope $(\Gamma_{660}) = 0$, -2.5, -5 MPa K^{-1}. Top row: isosurface of the composition with contour level $C = 0.5$. Middle row: polar slice of the composition. Bottom row: polar slice of the temperature.

Figure 16. Fraction of primordial dense material in the upper mantle with different buoyancy ratio (B) and Clapeyron slope at 660 km (Γ_{660}).

by the secondary plumes (Fig. 14d and e). Fig. 16 indicates that the fraction of primordial material in the upper mantle decreases by about 30 per cent when the Clapeyron slope increases strength from 0 to -2.5 MPa K^{-1}. Interestingly, a large Clapeyron slope of around -5.0 MPa K^{-1} triggers a double layering (plots g and h in Fig. 14). First, plumes rising from the bottom of the shell and downwellings sinking from the surface are stopped below and above the phase transition, respectively, inducing a stratification of the system, that is convection operates separately in the shells below and above the transition. As a consequence, the dense material is trapped below the phase transition. Second, because of this layering convection in the bottom shell is less vigorous (the thickness of

each subshells, hence the Rayleigh numbers, are smaller) which in turn increases the stability of the layer of dense material. Note, however, that such a large negative Clapeyron slope is not applicable to the Earth. If the dense reservoirs are more stable due to larger buoyancy ratio (Fig. 15), only a small amount of dense material is entrained upwards by plumes. This dense material is further filtered by the transition zone, provided that the Clapeyron slope at 660 km depth is large enough. A Clapeyron slope of -2.5 MPa K^{-1} can reduce the entrainment to the upper mantle by around 30 per cent to 40 per cent. Again, if the Clapeyron slope is too large, the system is stratified and all the dense material remains trapped below the phase transition.

4 CONCLUDING DISCUSSION

In this study, we perform numerical experiments of thermochemical mantle convection in 3-D spherical geometry to identify the parameters that control the thermochemical structure and dynamics of the system. Our findings generally show that the conclusions drawn from studies in 3-D Cartesian geometry (Deschamps & Tackley 2008, 2009), are also valid in 3-D spherical geometry. They also agree with previous experiments in 3-D-spherical geometry (McNamara & Zhong 2004). Our systematic search allows us to identify the parameter range needed to maintain reservoirs of dense material for a period of time comparable to the age of the Earth, without them mixing with the surrounding mantle.

Maintaining reservoirs of dense material requires both moderate chemical buoyancy ratio and a large thermal viscosity contrast. A

large buoyancy ratio leads to global chemical stratification of the system with a stable layer of dense material covering the CMB. This structure does not fit seismological observations, because it induces a discontinuity in the radial model of seismic velocity, which is not observed. Furthermore, the mantle beneath the discontinuity would appear to be homogeneous, whereas tomographic models report strong lateral variations. A low buoyancy ratio favours quick mixing between the dense and regular material, leading to a chemically homogeneous mantle. At least in the lowermost mantle, seismological observations imply the presence of strong chemical heterogeneities. For intermediate buoyancy ratios, reservoirs form due to the dense material being swept away from downwellings, but keeping them stable requires a large thermal viscosity contrast. Our study indicates that such structures may be obtained with a buoyancy ratio between 0.2 and 0.36 (which, if taking a superadiabatic jump of 2500 K, corresponds to a chemical density difference between 80 and 145 kg m^{-3}). This is in agreement with current estimates of density anomalies in the lower mantle (Trampert *et al.* 2004; Mosca *et al.* 2012). A large thermal viscosity contrast also helps in building long wavelength structures dominated by spherical harmonic degree 2. Note that (Tan *et al.* 2011) explored other combinations of parameters and found that higher bulk modulus also helps in keeping the reservoir stable and maintaining sharp edges.

Our numerical experiments further indicate that the volume fraction of dense material plays a second-order role in controlling the stability and structure of dense materials. This is consistent with previous analogue (Jaupart *et al.* 2007) and numerical (McNamara & Zhong 2004) experiments. Interestingly, if the thermal viscosity contrast and the buoyancy ratio both have intermediate values, the effect of the volume fraction is more pronounced. In the case of the Earth's mantle, the volume fraction of initial dense material is still poorly constrained. A crude estimate inferred from the volume of LLSVPs suggests a value in the range 1.5–3 per cent at the present day. This is consistent with with our results, which suggest that the most likely value of the volume fraction of dense material (in the sense that the reservoirs' geometry matches that of LLSVPs) is lower than 5 per cent. For these values, the initial thickness of the dense material is between 200 and 400 km, and the height of the dense reservoirs reaches 500–800 km above CMB, consistent with the height of LLSVPs observed by most of the tomography models (e.g. Masters *et al.* 2000; Houser *et al.* 2008; Ritsema *et al.* 2011).

More interestingly, our 3-D spherical experiments indicate that the volume fraction of dense material influences the distribution of plumes. For values of the volume fraction of 10 per cent and higher, plumes are located near the centre of the reservoirs and along central ridges. By contrast, for volume fractions less than 5 per cent, plumes are mostly located on the edges of the dense reservoirs. Reducing the volume fraction of dense material is therefore consistent with observation from palaeomagnetic data that suggest that plumes originate from the edges of LLSVPs (Burke & Torsvik 2004; Torsvik *et al.* 2008, 2010). Note that models that impose surface velocity from models of reconstructed plate motion (McNamara & Zhong 2005; Zhang *et al.* 2010; Bower *et al.* 2013) also reproduce some of the observed characteristics of LLSVPs, including locally sharp edges (Ni *et al.* 2002), and the concentration of plumes near the edges of the reservoirs (Torsvik *et al.* 2008, 2010). Therefore, to fit the shape of LLSVPs best and to explain the location of hotpots as reconstructed by palaeomagnetic data, the volume fraction of dense material should not be larger than 5 per cent, equivalent to an initial thickness of dense material of about 300 km.

Although a phase transition at 660 km acts as a filter for dense materials, the strong cold downwellings can cross this phase transition

and reach the CMB in most of the experiments we performed. The hot upwellings, on the contrary, are blocked below the phase transition, and smaller plumes are generated above the phase transition. The filtering of dense material depends on the value of the Clapeyron slope of this transition. For a Clapeyron slope of −2.5 MPa K^{-1}, which is the expected value for the transition from ringwoodite to perovskite and periclase, most of the dense material remains trapped below the phase transition, but a small fraction of dense material penetrates into the upper shell and is entrained upwards to the surface. Interestingly, numerical experiments in 3-D Cartesian geometry (Deschamps *et al.* 2011) have shown that the entrainment of dense material by upper mantle plumes is consistent with the geochemical signature of ocean island basalts. Larger values of the Clapeyron slope ($< −4$ MPa K^{-1}) lead to layered convection, and thus keep the primordial dense material in the lower mantle, favouring chemical layering at the bottom of the system. This does not fit the seismic observations for the Earth's mantle. Furthermore, such large values of the Clapeyron slope at 660 km are unrealistic in the case of the Earth's mantle. The real effect of the 660 km transition is further complicated by multiple phase transition around this depth. In addition, mineral physics experiments indicate that plumes, because they are hot, may experience an exothermic phase transition (Hirose 2002), thus cancelling or reducing the filtering effect of this transition. It is important to note, however, that a positive Clapeyron slope does not influence the stability of the reservoirs of dense material, which remains mainly controlled by the buoyancy ratio.

Chemical viscosity contrast (between dense and regular materials) has a limited effect on the stability of reservoirs. Increasing the chemical viscosity contrast leads to larger topography and a sharper compositional boundary, and induces less entrainment of dense material into the surrounding mantle. It does, however, have an effect on layer morphology, as previously noted by McNamara & Zhong (2004). They found that if the dense material is less viscous then it tends to form ridges, whereas if it is more viscous then it tends to form domes. Our results (Fig. 12) are broadly consistent with this although in detail our obtained morphologies are somewhat different because our model is compressible rather than Boussinesq as in McNamara & Zhong (2004).

A detailed comparison between the thermochemical structures predicted by our models and seismic tomography would require an accurate equation of state modelling and mineral physics data to convert our temperature and compositional distributions in seismic velocity anomalies, and appropriate filtering of these distributions to match the resolution of global tomographic models. This is beyond the scope of this paper, but general comments may be drawn from the spectral heterogeneity maps issued from our models. In global tomographic models the lowermost mantle is clearly dominated by large-scale structures (spherical harmonic degrees 6 and less). The mid mantle appear mostly homogeneous, and strong anomalies are observed again close to the surface. According to our model search, basal large-scale thermochemical structures (dominated by degree 2) can be obtained by models that include a moderate buoyancy ratio and a large thermal viscosity contrast (Figs 3 and 6). Such models further predict no chemical anomalies in the mid and small thermal anomalies in the mid mantle, which would lead to a seismically homogeneous mantle. Below the surface, the spreading of plumes induces strong temperature anomalies that may partly explain the observed tomography (another source of tomographic anomalies in the uppermost mantle that is not taken into account in our models is the dichotomy between oceans and continents, which persist down to about 300 km depth). Models with lower buoyancy ratio and/or smaller thermal viscosity contrasts, in which primordial and

regular materials mix efficiently, lead to thermochemical structures that are dominated by smaller scale anomalies throughout the mantle including in the mid-mantle (1st and 2nd row in Fig. 6), and are therefore unlikely to fit tomographic maps. Assuming that the primordial reservoirs are enriched in iron, a rough estimate of the seismic velocity anomaly generated by these reservoirs may further be calculated. Taking a superadiabatic jump of 2500 K (i.e. accounting for the adiabatic contribution, a total temperature increase around 3500 K), the lateral thermal anomalies predicted by our models with large-scale structures vary with depth and case (Fig. S2; see next paragraph for details of the calculations). For cases in which reservoirs of dense material are maintained, temperature anomalies are typically around ± 500 K. Assuming that the reservoirs of dense material are further enriched in iron by about 3 per cent compared to the surrounding material, as suggested by probabilistic tomography (Trampert *et al.* 2004; Mosca *et al.* 2012), and converting the thermochemical structure with sensitivities calculated by Deschamps *et al.* (2012) from an appropriate mineral physics data set, this would lead to shear wave velocity anomalies around -2.5 per cent, typical of what is observed in LLSVP.

We have further calculated the temperature excess in plumes for the cases discussed in this paper. Defining the plume boundary is subjective. Here, we used a definition similar to that of Labrosse (2002), which assume that a point is located within a plume if the temperature at this point is larger than

$$T_b(z) = T_m(z) + c \times (T_{\max}(z) - T_m(z)), \tag{8}$$

where $T_m(z)$ and $T_{\max}(z)$ are the horizontally averaged and maximum temperature at height z, and c a constant, which we fix here to $c = 0.5$, based on previous estimates in 3-D Cartesian geometry (see Supporting Information in Deschamps *et al.* 2011). We then define the average plume temperature and the excess temperature of plumes as

$$T_{\text{plume}}(z) = 0.5 \times (T_b(z) + T_{\max}(z)) \tag{9}$$

$$T_{\text{excess}} = T_{\text{plume}}(z) - T_m(z) \tag{10}$$

The excess temperatures at height $z = 0.90$ (corresponding to 290 km below the surface) are in the range of 250–400 K, depending on the cases. Supporting Information Fig. S2 shows radial profiles of the absolute maximum excess temperatures for selected cases. Several conclusions may be drawn from these profiles. For all the cases that can maintain stable primordial reservoirs, the excess temperature in the upper mantle does not vary substantially. In cases in which reservoirs are not stable, that is are entrained the upper mantle, the excess temperatures in the upper mantle increase. In the lower mantle: larger buoyancy ratios lead to smaller excess temperature, whereas larger thermal viscosity contrasts lead to smaller excess temperature. The volume fraction of primordial material mainly affects the depth at which the peak of excess temperature is located, with larger volume fractions leading to shallower depths. The excess temperature slightly decreases with chemical viscosity contrast. Finally, large values of the Clapeyron slope (i.e. -5.0 MPa K^{-1}) lead to small excess temperature, whereas small values of this parameter do not significantly affect the excess temperature.

Due to its large uncertainties, the phase change from perovskite to post-perovskite was not investigated in this study. This transition may, however, occur in Earth's lowermost mantle just above CMB (Murakami *et al.* 2004; Oganov & Ono 2004). Previous numerical studies suggested that this phase change may have important implications in terms of dynamics and evolution of the Earth's mantle (e.g. Nakagawa & Tackley 2004, 2005, 2006, 2011; Zhang & Zhong 2011; Samuel & Tosi 2012). Experimental studies (Yoshino & Yamazaki 2007; Hunt *et al.* 2009) and first principle calculations of atomic diffusion (Ammann *et al.* 2010) indicate that post-perovskite is less viscous than perovskite by a factor of $O(10^{-3})$ to $O(10^{-4})$. Since post-perovskite is most likely to lie outside dense reservoirs (because these reservoirs are hot, and thus outside the stability field of post-perovskite), the effect of chemical viscosity contrast, which we explored in this study, may be important in explaining the shape of LLSVPs. It has also been suggested that small lenses of post-perovskite may exist within the LLSVPs (e.g. Lay *et al.* 2006; Tackley *et al.* 2007). Due to its dependence on composition in oxides, iron-rich perovskite may be able to transform at higher temperature in LLSVPs than outside these regions. This would lead to the formation of iron-rich post-perovskite lenses, which have been proposed as a candidate to explain the ultra-low velocity zones observed by seismologists (Mao *et al.* 2006). Hence, finer models of lowermost mantle structure and dynamics would require accounting for the phase change of perovskite to post-perovskite. Previous studies (e.g. Nakagawa & Tackley 2011; Zhang & Zhong 2011; Samuel & Tosi 2012; Hunt *et al.* 2012) have found that it has a first-order effect on convective vigour and heat flow.

Seismological studies clearly show that cold slabs can reach the bottom of the mantle. These slabs bring recycled MORB into the lowermost mantle, which may accumulate there. This constitutes another possible source of chemical heterogeneity at the bottom of the mantle (e.g. Nakagawa *et al.* 2010). Furthermore, this recycled MORB may interact with the reservoirs of dense primordial material and modify the thermochemical structure of the lower mantle and its dynamics. The Basal Melange hypothesis (Tackley 2012) proposes that small fractions of MORB are regularly incorporated in pre-existing primordial reservoirs. High-resolution 2-D Cartesian models of thermochemical convection further show that small fractions of MORB are incorporated in primordial reservoirs and are subsequently partially re-entrained towards the surface by plumes generated at the top of the primordial reservoir (Li *et al.* 2014). In order to investigate the interaction of recycled MORB with primordial dense material, a three-compositional-component system is required (e.g. Nakagawa & Tackley 2014).

REFERENCES

Ammann, M., Brodholt, J. & Dobson, D., 2009. DFT study of migration enthalpies in MgSiO$_3$ perovskite, *Phys. Chem. Miner.,* **36**(3), 151–158.

Ammann, M., Brodholt, J., Wookey, J. & Dobson, D., 2010. First-principles constraints on diffusion in lower-mantle minerals and a weak D'' layer, *Nature,* **465**(7297), 462–465.

Austermann, J., Kaye, B.T., Mitrovica, J.X. & Huybers, P., 2014. A statistical analysis of the correlation between large igneous provinces and lower mantle seismic structure, *Geophys. J. Int.,* **197**(1), 1–9.

Bower, D.J., Gurnis, M. & Seton, M., 2013. Lower mantle structure from paleogeographically constrained dynamic Earth models, *Geochem. Geophys. Geosyst.,* **14**, 44–63.

Burke, K. & Torsvik, T.H., 2004. Derivation of large igneous provinces of the past 200 million years from long-term heterogeneities in the deep mantle, *Earth planet. Sci. Lett.,* **227**(3), 531–538.

Christensen, U., 1989. Models of mantle convection: one or several layers, *Phil. Trans. R. Soc. Lond., A.,* **328**(1599), 417–424.

Christensen, U.R. & Hofmann, A.W., 1994. Segregation of subducted oceanic crust in the convecting mantle, *J. geophys. Res.: Solid Earth (1978–2012),* **99**(B10), 19 867–19 884.

Davaille, A., 1999. Simultaneous generation of hotspots and superswells by convection in a heterogeneous planetary mantle, *Nature,* **402**(6763), 756–760.

Davies, D.R., Goes, S., Davies, J., Schuberth, B., Bunge, H.-P. & Ritsema, J., 2012. Reconciling dynamic and seismic models of Earth's lower mantle: the dominant role of thermal heterogeneity, *Earth planet. Sci. Lett.,* **353–354**(0), 253–269.

Deschamps, F. & Tackley, P.J., 2008. Searching for models of thermo-chemical convection that explain probabilistic tomography: I. Principles and influence of rheological parameters, *Phys. Earth planet. Inter.,* **171**(1), 357–373.

Deschamps, F. & Tackley, P.J., 2009. Searching for models of thermo-chemical convection that explain probabilistic tomography. II. Influence of physical and compositional parameters, *Phys. Earth planet. Inter.,* **176**(1), 1–18.

Deschamps, F. & Trampert, J., 2003. Mantle tomography and its relation to temperature and composition, *Phys. Earth planet. Inter.,* **140**(4), 277–291.

Deschamps, F., Kaminski, E. & Tackley, P.J., 2011. A deep mantle origin for the primitive signature of ocean island basalt, *Nat. Geosci.,* **4**(12), 879–882.

Deschamps, F., Cobden, L. & Tackley, P. J., 2012. The primitive nature of large low shear-wave velocity provinces, *Earth planet. Sci. Lett.,* **349–350,** 198–208.

Dziewonski, A.M. & Anderson, D.L., 1981. Preliminary reference Earth model, *Phys. Earth planet. Inter.,* **25**(4), 297–356.

Dziewonski, A.M., Lekic, V. & Romanowicz, B.A., 2010. Mantle Anchor Structure: an argument for bottom up tectonics, *Earth planet. Sci. Lett.,* **299**(1), 69–79.

Forte, A.M. & Mitrovica, J.X., 2001. Deep-mantle high-viscosity flow and thermochemical structure inferred from seismic and geodynamic data, *Nature,* **410**(6832), 1049–1056.

Gurnis, M. & Davies, G.F., 1986. The effect of depth-dependent viscosity on convective mixing in the mantle and the possible survival of primitive mantle, *Geophys. Res. Lett.,* **13**(6), 541–544.

He, Y. & Wen, L., 2012. Geographic boundary of the Pacific Anomaly and its geometry and transitional structure in the north, *J. geophys. Res.: Solid Earth (1978–2012),* **117**(B9), doi:10.1029/2012JB009436, 2012.

Hernlund, J.W. & Houser, C., 2008. On the statistical distribution of seismic velocities in Earth's deep mantle, *Earth planet. Sci. Lett.,* **265**(3), 423–437.

Hirose, K., 2002. Phase transitions in pyrolitic mantle around 670-km depth: implications for upwelling of plumes from the lower mantle, *J. geophys. Res.: Solid Earth (1978–2012),* **107**(B4), doi:10.1029/2001JB000597.

Holzapfel, C., Rubie, D.C., Frost, D.J. & Langenhorst, F., 2005. Fe-Mg inter-diffusion in (Mg, Fe) SiO$_3$ perovskite and lower mantle reequilibration, *Science,* **309**(5741), 1707–1710.

Houser, C., Masters, G., Shearer, P. & Laske, G., 2008. Shear and compressional velocity models of the mantle from cluster analysis of long-period waveforms, *Geophys. J. Int.,* **174**(1), 195–212.

Hunt, S.A., Weidner, D.J., Li, L., Wang, L., Walte, N.P., Brodholt, J.P. & Dobson, D.P., 2009. Weakening of calcium iridate during its transformation from perovskite to post-perovskite, *Nat. Geosci.,* **2**(11), 794–797.

Hunt, S.A., Davies, D.R., Walker, A.M., McCormack, R.J., Wills, A.S., Dobson, D.P. & Li, L., 2012. On the increase in thermal diffusivity caused by the perovskite to post-perovskite phase transition and its implications for mantle dynamics, *Earth planet. Sci. Lett.,* **319**, 96–103.

Ishii, M. & Tromp, J., 1999. Normal-mode and free-air gravity constraints on lateral variations in velocity and density of Earth's mantle, *Science,* **285**(5431), 1231–1236.

Jaupart, C., Molnar, P. & Cottrell, E., 2007. Instability of a chemically dense layer heated from below and overlain by a deep less viscous fluid, *J. Fluid Mech.,* **572,** 433–470.

Kageyama, A. & Sato, T., 2004. Yin-Yang grid: an overset grid in spherical geometry, *Geochem. Geophys. Geosyst.,* **5**(9), doi:10.1029/2004GC000734.

Karato, S.-I. & Karki, B.B., 2001. Origin of lateral variation of seismic wave velocities and density in the deep mantle, *J. geophys. Res.: Solid Earth (1978–2012),* **106**(B10), 21 771–21 783.

Kellogg, L.H., Hager, B.H. & van der Hilst, R.D., 1999. Compositional stratification in the deep mantle, *Science,* **283**(5409), 1881–1884.

Kennett, B., 1991. Iaspei 1991 seismological tables, *Terra Nova,* **3**(2), 122–122.

Labrosse, S., 2002. Hotspots, mantle plumes and core heat loss, *Earth planet. Sci. Lett.,* **199**(1), 147–156.

Labrosse, S., Hernlund, J. & Coltice, N., 2007. A crystallizing dense magma ocean at the base of the EarthÕs mantle, *Nature,* **450**(7171), 866–869.

Lay, T., Hernlund, J., Garnero, E.J. & Thorne, M.S., 2006. A post-perovskite lens and D'' heat flux beneath the central Pacific, *Science,* **314**(5803), 1272–1276.

Lee, C.-T.A., Luffi, P., Höink, T., Li, J., Dasgupta, R. & Hernlund, J., 2010. Upside-down differentiation and generation of a primordial lower mantle, *Nature,* **463**(7283), 930–933.

Li, X.-D. & Romanowicz, B., 1996. Global mantle shear velocity model developed using nonlinear asymptotic coupling theory, *J. geophys. Res.: Solid Earth (1978–2012),* **101**(B10), 22 245–22 272.

Li, M., McNamara, A.K. & Garnero, E.J., 2014. Chemical complexity of hotspots caused by cycling oceanic crust through mantle reservoirs, *Nat. Geosci.,* **7,** 366–370.

Machetel, P. & Weber, P., 1991. Intermittent layered convection in a model mantle with an endothermic phase change at 670 km, *Nature,* **350,** 55–57.

Mao, W.L. *et al.*, 2006. Iron-rich post-perovskite and the origin of ultralow-velocity zones, *Science,* **312**(5773), 564–565.

Masters, G., Laske, G., Bolton, H. & Dziewonski, A., 2000. The relative behavior of shear velocity, bulk sound speed, and compressional velocity in the mantle: implications for chemical and thermal structure, in *Earth's Deep Interior: Mineral Physics and Tomography from the Atomic to the Global Scale,* pp. 63–87, eds Karato, S., Forte, A., Liebermann, R., Masters, G. & Stixrude, L., John Wiley and Sons.

McNamara, A.K. & Zhong, S., 2004. Thermochemical structures within a spherical mantle: superplumes or piles?, *J. geophys. Res.: Solid Earth (1978–2012),* **109**(B7), doi:10.1029/2003JB002847.

McNamara, A.K. & Zhong, S., 2005. Thermochemical structures beneath Africa and the Pacific Ocean, *Nature,* **437**(7062), 1136–1139.

Mosca, I., Cobden, L., Deuss, A., Ritsema, J. & Trampert, J., 2012. Seismic and mineralogical structures of the lower mantle from probabilistic tomography, *J. geophys. Res.: Solid Earth (1978–2012),* **117**(B6), doi:10.1029/2011JB008851.

Murakami, M., Hirose, K., Kawamura, K., Sata, N. & Ohishi, Y., 2004. Post-perovskite phase transition in MgSiO$_3$, *Science,* **304**(5672), 855–858.

Nakagawa, T. & Tackley, P.J., 2004. Effects of a perovskite-post perovskite phase change near core-mantle boundary in compressible mantle convection, *Geophys. Res. Lett.,* **31**(16), doi:10.1029/2004GL020648.

Nakagawa, T. & Tackley, P.J., 2005. The interaction between the post-perovskite phase change and a thermo-chemical boundary layer near the core–mantle boundary, *Earth planet. Sci. Lett.,* **238**(1), 204–216.

Nakagawa, T. & Tackley, P.J., 2006. Three-dimensional structures and dynamics in the deep mantle: effects of post-perovskite phase change and deep mantle layering, *Geophys. Res. Lett.,* **33**(12), doi::10.1029/2006GL025719.

Nakagawa, T. & Tackley, P.J., 2011. Effects of low-viscosity post-perovskite on thermo-chemical mantle convection in a 3-D spherical shell, *Geophys. Res. Lett.,* **38**(4), doi:10.1029/2010GL046494.

Nakagawa, T. & Tackley, P.J., 2014. Influence of combined primordial layering and recycled MORB on the coupled thermal evolution of Earth's mantle and core, *Geochem. Geophys. Geosyst.,* **15,** 619–633.

Nakagawa, T., Tackley, P.J., Deschamps, F. & Connolly, J.A., 2010. The influence of MORB and harzburgite composition on thermo-chemical mantle convection in a 3-D spherical shell with self-consistently calculated mineral physics, *Earth planet. Sci. Lett.,* **296**(3), 403–412.

Ni, S., Tan, E., Gurnis, M. & Helmberger, D., 2002. Sharp sides to the African superplume, *Science,* **296**(5574), 1850–1852.

Oganov, A.R. & Ono, S., 2004. Theoretical and experimental evidence for a post-perovskite phase of MgSiO$_3$ in Earth's D'' layer, *Nature,* **430**(6998), 445–448.

Oldham, D. & Davies, J.H., 2004. Numerical investigation of layered convection in a three-dimensional shell with application to planetary mantles, *Geochem. Geophys. Geosyst.,* **5**(12), Q12C04, doi:10.1029/2003GC000603.

Ritsema, J., Deuss, A., Van Heijst, H. & Woodhouse, J., 2011. S40RTS: a degree-40 shear-velocity model for the mantle from new Rayleigh wave dispersion, teleseismic traveltime and normal-mode splitting function measurements, *J. geophys. Res.,* **184**(3), 1223–1236.

Saltzer, R., Hilst, R.V.D. & Karason, H., 2001. Comparing p and s wave heterogeneity in the mantle, *Geophys. Res. Lett.,* **28**(7), 1335–1338.

Samuel, H. & Tosi, N., 2012. The influence of post-perovskite strength on the Earth's mantle thermal and chemical evolution, *Earth planet. Sci. Lett.,* **323**, 50–59.

Schuberth, B., Bunge, H.-P. & Ritsema, J., 2009. Tomographic filtering of high-resolution mantle circulation models: Can seismic heterogeneity be explained by temperature alone?, *Geochem. Geophys. Geosyst.,* **10**(5), doi:10.1029/2009GC002401.

Schuberth, B.S., Zaroli, C. & Nolet, G., 2012a. Synthetic seismograms for a synthetic Earth: long-period P-and S-wave traveltime variations can be explained by temperature alone, *Geophys. J. Int.,* **188**(3), 1393–1412.

Schuberth, Y., Richtler, T., Hilker, M., Salinas, R., Dirsch, B. & Larsen, S.S., 2012b. Dynamics of the NGC 4636 globular cluster system II. Improved constraints from a large sample of globular cluster velocities, *Astronomy & Astrophysics*, **544**, doi:10.1051/0004-6361/201015038.

Solomatov, V.S. & Stevenson, D.J., 1993. Suspension in convective layers and style of differentiation of a terrestrial magma ocean, *J. geophys. Res.: Planets (1991–2012),* **98**(E3), 5375–5390.

Su, W.-j., Woodward, R.L. & Dziewonski, A.M., 1994. Degree 12 model of shear velocity heterogeneity in the mantle, *J. geophys. Res.: Solid Earth (1978–2012),* **99**(B4), 6945–6980.

Tackley, P.J., 1996. On the ability of phase transitions and viscosity layering to induce long wavelength heterogeneity in the mantle, *Geophys. Res. Lett.,* **23**(15), 1985–1988.

Tackley, P.J., 1998. Three-dimensional simulations of mantle convection with a thermo-chemical basal boundary layer: D, *Core-Mantle Bound. Reg., Geodyn. Ser.* **28**, 231–253.

Tackley, P.J., 2002. Strong heterogeneity caused by deep mantle layering, *Geochem. Geophys. Geosyst,* **3**(4), 1024, doi:10.1029/2001GC000167.

Tackley, P.J., 2008. Modelling compressible mantle convection with large viscosity contrasts in a three-dimensional spherical shell using the Yin-Yang grid, *Phys. Earth planet. Inter.,* **171**(1), 7–18.

Tackley, P.J., 2012. Dynamics and evolution of the deep mantle resulting from thermal, chemical, phase and melting effects, *Earth-Sci. Rev.,* **110**(1), 1–25.

Tackley, P.J. & King, S.D., 2003. Testing the tracer ratio method for modeling active compositional fields in mantle convection simulations, *Geochem. Geophys. Geosyst.,* **4**(4), 8302, doi:10.1029/2001GC000214.

Tackley, P.J., Stevenson, D.J., Glatzmaier, G.A. & Schubert, G., 1993. Effects of an endothermic phase transition at 670 km depth in a spherical model of convection in the Earth's mantle, *Nature,* **361**(6414), 699–704.

Tackley, P.J., Nakagawa, T. & Hernlund, J.W., 2007. Influence of the post-perovskite transition on thermal and thermo-chemical mantle convection, *Post-perovskite: The Last Mantle Phase Transition,* pp. 229–247, eds Hirose, K., Brodholt, J., lay, T. & yuen, D., John Wiley and Sons.

Tan, E., Leng, W., Zhong, S. & Gurnis, M., 2011. On the location of plumes and lateral movement of thermochemical structures with high bulk modulus in the 3-D compressible mantle, *Geochem. Geophys. Geosyst.,* **12**(7), doi:10.1029/2011GC003665.

Tolstikhin, I., Kramers, J. & Hofmann, A., 2006. A chemical Earth model with whole mantle convection: the importance of a core–mantle boundary layer (D'') and its early formation, *Chemical geology,* **226**(3), 79–99.

Torsvik, T.H., Smethurst, M.A., Burke, K. & Steinberger, B., 2006. Large igneous provinces generated from the margins of the large low-velocity provinces in the deep mantle, *Geophys. J. Int.,* **167**(3), 1447–1460.

Torsvik, T.H., Steinberger, B., Cocks, L.R.M. & Burke, K., 2008. Longitude: linking Earth's ancient surface to its deep interior, *Earth planet. Sci. Lett.,* **276**(3), 273–282.

Torsvik, T.H., Burke, K., Steinberger, B., Webb, S.J. & Ashwal, L.D., 2010. Diamonds sampled by plumes from the core-mantle boundary, *Nature,* **466**(7304), 352–355.

Trampert, J., Deschamps, F., Resovsky, J. & Yuen, D., 2004. Probabilistic tomography maps chemical heterogeneities throughout the lower mantle, *Science,* **306**(5697), 853–856.

van Summeren, J., van den Berg, A. & van der Hilst, R., 2009. Upwellings from a deep mantle reservoir filtered at the 660 km phase transition in thermo-chemical convection models and implications for intra-plate volcanism, *Phys. Earth planet. Inter.,* **172**(3), 210–224.

Wang, Y. & Wen, L., 2007. Geometry and P and S velocity structure of the African Anomaly, *J. geophys. Res.: Solid Earth (1978–2012),* **112**(B5), doi::10.1029/2006JB004483.

Weinstein, S.A., 1992. Induced compositional layering in a convecting fluid layer by an endothermic phase transition, *Earth planet. Sci. Lett.,* **113**(1), 23–39.

Wolstencroft, M. & Davies, J., 2011. Influence of the ringwoodite-perovskite transition on mantle convection in spherical geometry as a function of Clapeyron slope and Rayleigh number, *Solid Earth Discuss.,* **3**(2), 713–741.

Yamazaki, D. & Karato, S.-i., 2001. Some mineral physics constraints on the rheology and geothermal structure of Earths lower mantle, *Am. Mineral.,* **86**(4), 385–391.

Yoshino, T. & Yamazaki, D., 2007. Grain growth kinetics of CaIrO$_3$ perovskite and post-perovskite, with implications for rheology of D'' layer, *Earth planet. Sci. Lett.,* **255**(3), 485–493.

Zhang, N. & Zhong, S., 2011. Heat fluxes at the earth's surface and core–mantle boundary since Pangea formation and their implications for the geomagnetic superchrons, *Earth planet. Sci. Lett.,* **306**(3–4), 205–216.

Zhang, N., Zhong, S., Leng, W. & Li, Z.-X., 2010. A model for the evolution of the Earth's mantle structure since the Early Paleozoic, *J. geophys. Res.: Solid Earth (1978–2012),* **115**(B6), doi:10.1029/2009JB006896.

SUPPORTING INFORMATION

Additional Supporting Information may be found in the online version of this article:

Figure S1. 1-D viscosity profile for the reference case. The black, blue, and red curves show the horizontally averaged viscosity, the maximum and minimum viscosity, respectively.

Figure S2. Radial profiles of the excess temperature in plumes for the cases in Table 2 (http://mnras.oxfordjournals.org/lookup/suppl/doi:10.1093/mnras/ggu295/-/DC1).

Please note: Oxford University Press is not responsible for the content or functionality of any supporting materials supplied by the authors. Any queries (other than missing material) should be directed to the corresponding author for the article.

Online supplementary information

Yang Li & Paul.J.Tackley
Institute of geophysics, department of Earth Sciences, ETH Zurich, Switzerland

Frederic Deschamps
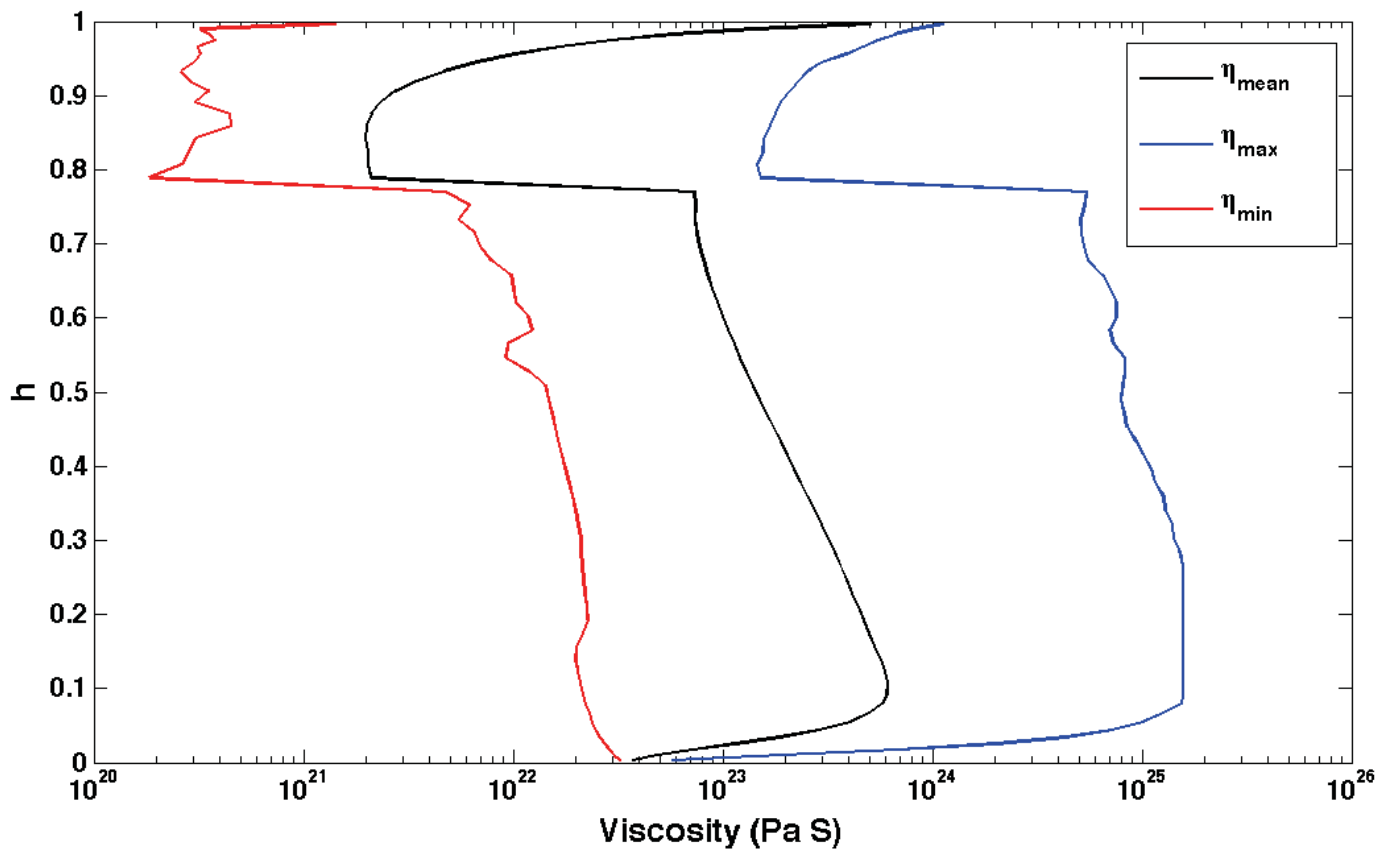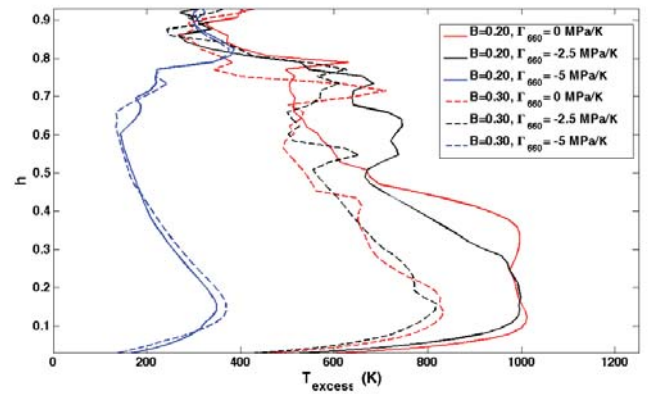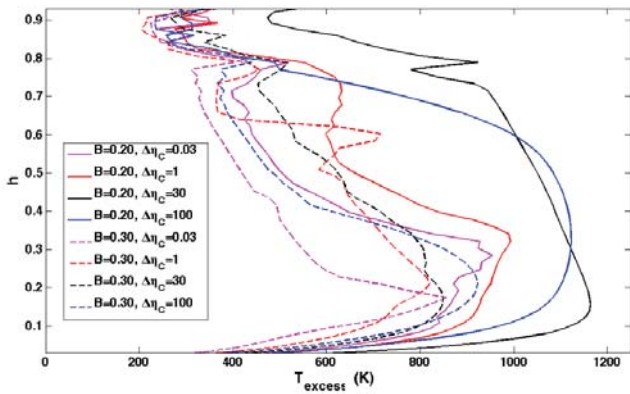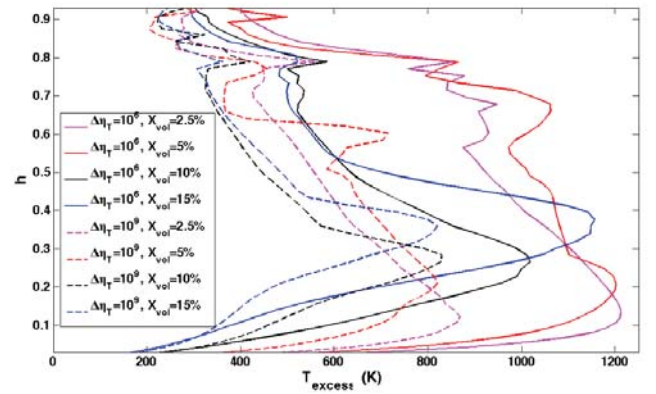Institute of Earth Sciences, Academia Sinica, Taipei, Taiwan

Figure S1. 1-D viscosity profile for the reference case. The black, blue, and red curves show the horizontally averaged viscosity, the maximum and minimum viscosity, respectively.
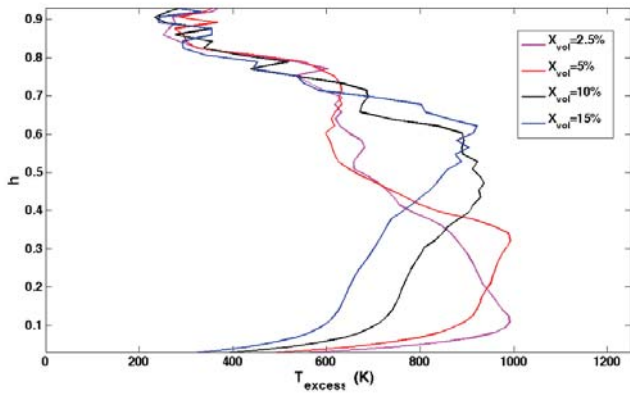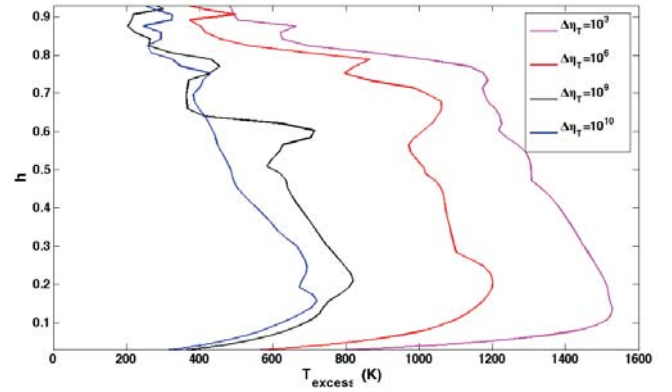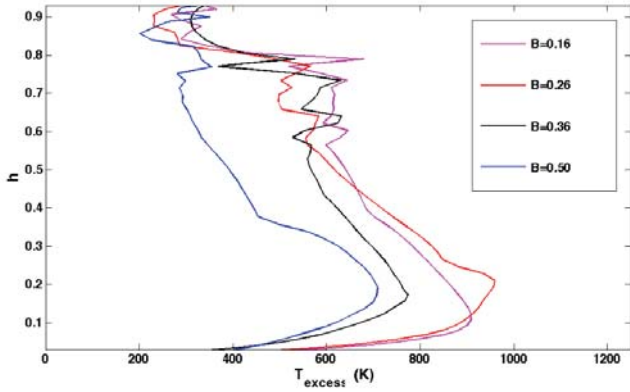
Figure S2. Radial profiles of the excess temperature in plumes for the cases in table 2.